Journal of Polymers and the Environment
https://doi.org/10.1007/s10924-025-03521-8

ORIGINAL PAPER

# UiO-66 Metal-organic Framework (MOF) as an Osteogenic Stimulant in the Poly-3-hydroxybutyrate-zein/UiO-66 Electrospun Composite Scaffold for Bone Tissue Engineering Applications

**Saeid Ghasemi**[1] · **Mahdie Esmaeili**[1] · **Mohammad Dinari**[2] · **Arezou Dabiri**[3] · **Saeed Karbasi**[1]

Accepted: 29 January 2025

## Abstract

Metal-organic frameworks have recently become popular in biomedical applications due to their high surface areas, porosity, suitable mechanical properties, controlled degradability, and selective compositions. Among them, UiO-66 is particularly noteworthy for its exceptional stability, biodegradability, low toxicity, and osteogenic properties. Herein, UiO-66 was synthesized via a solvothermal method and characterized employing FTIR, XRD, FESEM, and TEM analyses. Subsequently, poly-3-hydroxybutyrate-zein/UiO-66 electrospun composite scaffolds were fabricated. Regarding the SEM, mechanical analyses, and water contact angle results, the scaffold containing 2 wt% UiO-66 exhibited the optimum characteristic. EDS and TEM examinations confirmed UiO-66's presence and distribution, TGA validated its claimed amount in the scaffold, and FTIR revealed the possible interactions between ingredients. Incorporating 2 wt% UiO-66 reduced the fiber diameter and water contact angle by about 54 nm and 20°, respectively, while increasing surface roughness and crystallinity. UiO-66 significantly enhanced ultimate tensile stress and Young's modulus by approximately 90% and 101%, respectively. It also boosted the biomineralization of the scaffold and hastened the degradation rate. Eventually, adding UiO-66 led to noticeable increases in viability, proliferation, attachment, ALP activity, and ECM mineralization, as well as upregulation of COLI, RUNX2, and OCN genes of MG-63 cells seeded on the scaffolds. In conclusion, incorporating UiO-66 not only reinforced the composite scaffold but also stimulated osteogenesis, making it an advantageous candidate for bone tissue engineering applications.

**Keywords** UiO-66 · Metal-organic Framework (MOF) · Poly-3-hydroxybutyrate (PHB) · Zein · Protein · Bone Tissue Engineering · Osteogenesis

## Introduction

In the U.S., age-related bone disorders are projected to rise to 3 million by 2025, and in Europe, fracture cases are expected to increase by 28% between 2010 and 2025. Thus, effective treatments for bone diseases are clinically significant [1]. Autogenous, allogeneic, and xenogeneic bone grafts, as the traditional methods, face issues like limited availability, pathogens transmission, and immune rejection. Artificial implants, despite good biocompatibility, often fail in cases of tumors, inflammation, or infections. Also, some bone diseases require functionalized particles for effective treatment [2, 3]. As a promising alternative to tackle these challenges and meet clinical needs, bone tissue engineering, with three fundamental components, including scaffolds, seeded cells, and bioenvironmental factors, has gained

---

Saeid Ghasemi and Mahdie Esmaeili contributed equally.

✉ Saeed Karbasi
karbasi@med.mui.ac.ir

[1] Department of Biomaterials and Tissue Engineering, School of Advanced Technologies in Medicine, Isfahan University of Medical Sciences, Isfahan, Iran

[2] Department of Chemistry, Isfahan University of Technology, Isfahan 84156-83111, Islamic Republic of Iran

[3] Applied Physiology Research Center, Cardiovascular Research Institute, Isfahan University of Medical Sciences, Hezarjerib Ave, Isfahan 8174673461, Iran

considerable interest [4]. By offering mechanical support and a favorable environment for cell attachment, proliferation, and differentiation, the scaffold generally imitates the extracellular matrix (ECM) throughout the tissue regeneration process [5]. Among the various methods of creating scaffolds, electrospinning has garnered significant attention due to its cost-effectiveness, simplicity, efficiency, and ability to construct three-dimensional (3D) networks with high surface area, different morphologies, and interconnected pores for nutrient transportation, cell migration, and controlled drug release. These characteristics allow the electrospun scaffolds to closely resemble the ECM, facilitating cell signaling [6–8]. The choice of raw materials for scaffold construction is another critical factor significantly impacting their final characteristics. Desired properties, such as hydrophilicity and biodegradability, make polymers an advantageous option. One of the frequently used polymers for fabricating electrospun scaffolds is poly-3-hydroxybutyrate (PHB), which is notable for its mechanical properties, biodegradability, biocompatibility, semicrystalline structure, and excellent electrospinning capability [7, 9]. PHB also has a piezoelectric crystalline phase and can generate electrical charges upon mechanical stress, which is useful in bone tissue regeneration because it can electrically stimulate cells [10]. However, its application in tissue engineering is limited due to its hydrophobicity, stiffness, brittleness, high crystallinity, and slow degradation rate [9, 11, 12]. Potential methods to improve PHB's properties for tissue engineering applications include alloying with natural polymers, such as zein [7], chitosan [13], keratin [14], lignin [15], gelatin [16], and starch [17]; compositing PHB with nanoparticles, such as multiwalled carbon nanotube [11], halloysite nanotube [18], graphene oxide [19], chitosan nanoparticles [20], ECM nanoparticles [21], and bioglasses [22, 23]; and applying PHB as a coating for ceramic-based scaffolds [24, 25].

Compared to animal-derived proteins, proteins derived from plants are more accessible, cost-effective, biodegradable, and antioxidative, with less immunogenic response and disease transmission. These proteins mimic the native ECM's chemical composition and structure [26]. Zein, constituting about 80% of maize protein and 44–79% of endosperm protein, was designated "generally recognized as safe" by the U.S. Food and Drug Administration in 1985. Rich in hydrophobic amino acids like leucine (20%), proline (10%), and alanine (10%), and containing some polar residues like glutamine (21–26%), making zein an amphiphilic protein. Its flexibility, low cytotoxicity, biocompatibility, biodegradability, excellent compatibility with ECM constituents, antioxidant activity, and cell compatibility of breakdown products have made zein ideal for tissue engineering scaffolds [7, 8, 27, 28]. Our previous research revealed that incorporating 10 wt% zein into PHB electrospun scaffolds reduced fiber diameter while enhancing mechanical properties. Additionally, zein imparted antioxidant activity to the scaffolds and enhanced cell attachment, viability, and differentiation [7]. Although zein-containing fibers have advantageous properties, their mechanical strength limits their use in bone tissue engineering. Nevertheless, this limitation can be addressed by composing them with a reinforcing phase.

Metal-organic frameworks (MOFs) are crystalline compounds composed of metal ions or clusters linked by organic ligands. Large specific surface area, high and tunable porosity, superior biocompatibility, and intrinsic biodegradability are among the benefits that have rendered them appropriate for tissue engineering and regenerative medicine [4, 29–32]. In bone tissue engineering, MOFs have attracted significant interest, whether used on their own or as carriers for drugs. Their porous structure and mechanical properties are beneficial for cell adhesion and have been shown to promote angiogenesis. In the case of osteoblasts, MOFs enhance the expression of osteogenic genes, increase intracellular calcium deposition, and expedite ECM mineralization. Conversely, MOFs inhibit the size and function of osteoclasts [33].

Interest in zirconium (Zr)-based MOFs for biomedical applications has grown recently. Zr-containing biomaterials are extensively used in orthopedic and dental implants due to Zr's ability to stimulate osteoblast attachment, proliferation, differentiation, and osteogenic gene expression, enhancing mineralization. The human body contains about 300 mg of Zr, with a recommended daily intake of 4.15 mg [4, 29, 34]. UiO-66, UiO stands for Universitetet i Oslo, is a Zr-based structure first introduced by Cavka et al. in 2008 [35]. It is composed of octahedral $Zr_6O_4(OH)_4$ units and terephthalic acid [(1,4-benzene dicarboxylate (BDC)], in which each octahedral cluster is connected to 12 adjacent units via BDC, acting as organic ligands. UiO-66 has exhibited superior mechanical, thermal, acidic, aqueous, and water vapor stability due to its strong Zr-O bonds. It is also recognized as a bio-safe MOF, maintaining high cell viability at concentrations up to 800 mg/l [30, 31, 36–38]. Karakecili et al. [38] explored the use of UiO-66 in transporting fosfomycin and promoting osteogenesis within 3D chitosan scaffolds created via wet spinning. Their findings indicated enhanced compressive strength, water uptake, and osteogenic differentiation due to UiO-66 incorporation. Jarai et al. [39] assessed the potential of UiO-66 MOF as a vehicle for pulmonary drug delivery. The study found that UiO-66 exhibited pH-dependent stability, remaining stable under extracellular conditions while degrading within intracellular environments. Additionally, the UiO-66 MOF showed high biocompatibility and low cytotoxicity both in vitro and in vivo. Sadek et al. [4] examined UiO-66 as a scaffold, evaluating its biocompatibility and osteogenic potential in vitro and in vivo using a rabbit femoral condyle model. UiO-66 demonstrated excellent cytocompatibility and hemocompatibility, stimulating in vitro osteoblast functions and in vivo osteogenesis. This led to significant osteoid tissue and collagen deposition and upregulation of osteocalcin and osteopontin in vivo.

The mentioned studies suggest that incorporating UiO-66 MOF into bone tissue engineering scaffolds could improve the scaffold's osteogenic properties. However, to the best of the authors' knowledge, there has been no investigation into incorporating UiO-66 in the PHB-zein scaffold, particularly for use in bone tissue engineering. According to the literature, adding UiO-66 to PHB-zein fibers is expected to not only improve mechanical properties but also enhance its osteogenic characteristics. This study aimed to synthesize and characterize UiO-66 particles using a solvothermal protocol and then fabricate electrospun composite scaffolds using PHB, zein, and UiO-66 MOF. Eventually, structural, physical, chemical, and mechanical properties, as well as in vitro degradation behavior, bioactivity evaluation, and in vitro cellular behavior utilizing MG-63 osteoblast cells, were examined.

## Materials and Methods

### Materials

PHB (CAS number: 29435-48-1) and zein (CAS number: 9010-66-6) powders were purchased from Sigma Aldrich (USA). CDH (India) provided the trifluoroacetic acid (TFA; CAS number: 76-05-1) and acetic acid. For UiO-66 synthesis, zirconium tetrachloride, BDC, N, N-Dimethylformamide (DMF), benzoic acid, and hydrochloric acid were acquired from Merck (Germany), and methanol was purchased from Sigma-Aldrich (USA). For in vitro analyses, phosphate-buffered saline (PBS), simulated body fluid (SBF), Dulbecco Modified Eagle Medium (DMEM) + Glutamax (Low Glucose), Penicillin-streptomycin, trypsin EDTA 0.025%, and 3-(4,5-dimethylthiazol-2-yl)−2,5-diphenyl tetrazolium bromide (MTT) assay kit were provided by Bio-idea (Iran). Moreover, the following materials were purchased from the mentioned suppliers: Alizarin Red S from Sigma-Aldrich (USA), the alkaline phosphatase (ALP) assay kit from Darman-Kave (Iran), dimethyl sulfoxide (DMSO) from Pars Azmoon (Iran), total ribonucleic acid (RNA) extraction kit from Parstous (Iran), complementary deoxyribonucleic acid (cDNA) synthesis kit from Addbio (Korea), RealQplus 2× Masret Mix Green from Ampliqon (Denmark), glutaraldehyde (25% aqueous solution) from Sigma-Aldrich (USA), Ethanol from Merck (Germany), Triton X-100 from Arman Sina Chemical (Iran), 4′,6-diamidino-2-phenylindole (DAPI) from Sigma-Aldrich (USA), and MG-63 osteoblast cell line from Pasteur Institute (Iran).

**Table 1** Abbreviations and compositions of the fabricated electrospun scaffolds

| Scaffold abbreviation | PHB content (wt/v%) | Zein content (wt%) | UiO-66 content (wt%) |
|---|---|---|---|
| PZ | 9 | 10 | 0 |
| PZ-0.5U | 9 | 10 | 0.5 |
| PZ-1U | 9 | 10 | 1 |
| PZ-2U | 9 | 10 | 2 |

### UiO-66 Synthesis

UiO-66 MOF was synthesized using a solvothermal method, as described previously [40]. Briefly, 1.00 g (4.29 mmol) zirconium tetrachloride, 0.675 g (4.06 mmol) BDC, 7.89 g benzoic acid (64.6 mmol), and 712 µl (8.54 mmol) hydrochloric acid were ultrasonically dissolved in 78 ml (1 mol) DMF. The reaction mixture was then transferred to a Teflon-lined stainless-steel autoclave and heated to 120 °C for 48 h. After cooling down to room temperature, the product was separated using centrifugation at 6000 RPM for 15 min. Subsequently, the resulting white powder of UiO-66 was washed multiple times with DMF and methanol and eventually dried at 80 °C in a vacuum oven overnight.

### Fabrication of Electrospun Scaffolds

In accordance with our previous research [7], 0.09 g PHB powder and 0.009 g zein powder simultaneously were dissolved in 0.9 ml TFA and stirred for 1 h at 45 °C. Next, three different weight concentrations of 0.5, 1, and 2 wt% of UiO-66 were sonicated, using an ultrasonic bath, in 0.1 ml acetic acid for 30 min. The resulting suspension was mixed with as-prepared PHB-zein alloy and stirred for 30 min at room temperature to form a composite of PHB-zein/UiO-66. The final solution was drawn into a 1 ml syringe equipped with a 23 G needle. The electrospinning process was carried out under optimal conditions using an applied voltage of 23 kV at a distance of 23 cm and a feed rate of 0.004 ml/min. These parameters resulted in the formation of uniform, bead-free fibers with a consistent Taylor cone and a continuous electrospinning process devoid of droplet formation. The abbreviations for each group of scaffolds with varying UiO-66 contents are listed in Table 1.

### Characterization of the Synthesized UiO-66 Particles

The synthesized UiO-66 was analyzed for its structure and morphology employing a variety of techniques, including Fourier transform infrared spectroscopy (FTIR), X-ray diffraction (XRD), field emission scanning electron microscopy (FESEM), and transmission electron microscopy (TEM). FTIR spectra were collected in transmittance mode using a Jasco 6300 spectrophotometer (Germany) in the wavenumber range of 4000–350 $cm^{-1}$. XRD pattern was recorded at room temperature with a Bruker D8 Advanced diffractometer (Japan) over $2\theta = 5–35°$. The step size and time interval were set to be 0.05° and 1.5 s, respectively, and the equipment included a position-sensitive detector utilizing Cu Kα radiation ($\lambda = 0.15406$ nm) at an operating voltage of 40 kV. In order to capture FESEM images of the UiO-66 MOF, the particles were coated with gold using a BalTec SCD005 machine, followed by imaging employing FESEM (TESCAN, MIRA3 Brno/Czech Republic) with an operating voltage of 15 kV. To take TEM images, the UiO-66 particles were suspended in deionized distilled water and subjected to ultrasound. The resulting solution was then placed on a carbon film with a copper grid and assessed using a Philips EM 208 S TEM (Netherlands).

## Evaluation of the Fabricated Scaffold's Morphology

### Scanning Electron Microscopy (SEM)

The morphology of all the fabricated scaffolds' fibers was investigated using SEM (LEO 1430 VP/Germany). The samples were prepared by cutting them into 1 × 1 $cm^2$ squares and coating them with a gold layer using an Emitech SC7620 Sputter Coater (Quorum Technologies, UK). Images were captured at various magnifications with an operating voltage of 10.0 kV. The average diameter and distribution of the fibers were measured by analyzing 30 fibers randomly selected from each group using ImageJ software (National Institutes of Health and Laboratory for Optical and Computational Instrumentation, USA). Given that the electrospun scaffolds consist of multiple layers, each layer exhibits a distinct porosity. The porosity percentage of the three surface layers was determined through image analysis using MATLAB (R2019a) software. This method is explained in detail by Ghasemi-Mobarakeh et al. [41]. Briefly, three thresholds were applied to convert the SEM image to a binary format across the three layers based on the mean and standard deviation of the image pixel values. In the binary representation of each layer, the fibers are depicted as white areas, while the empty spaces are represented by black regions. The porosity in each binary image can be calculated using Eq. (1), where n is the number of white pixels, N is the total number of pixels in the binary image, and P is the porosity percentage of the binary image.

$$P = \left(1 - \frac{n}{N}\right) \times 100 \tag{1}$$

### Energy Dispersive X-ray Spectroscopy (EDS) Mapping

To identify the presence and distribution of UiO-66 within the electrospun composite scaffolds, an EDS mapping analysis of the Zr chemical element was conducted on the PZ-0.5U, PZ-1U, and PZ-2U samples using an Apollo X Silicon Drift Detector.

### TEM

TEM images can be used to confirm the incorporation of UiO-66 particles within the fibers of the composite scaffolds. To achieve this, one layer of the PZ-2U fibers was electrospun onto a copper grid on the collector surface, and subsequent TEM images were taken from the grid using a Philips EM 208 S (Netherlands).

### Atomic Force Microscopy (AFM)

AFM analysis was performed (Ara-Pajooh, Iran) to evaluate and compare the surface roughness of the PZ and PZ-2U scaffolds and assess the impact of UiO-66 on the scaffolds' roughness. Images were obtained from a 15 × 15 $\mu m^2$ area, and the roughness parameters Ra and Rq (Rms) were recorded. Ra represents the average surface roughness, while Rq denotes the root mean square roughness.

## FTIR

In order to study the functional groups of the components, possible chemical interactions, and verify the presence of PHB, zein, and UiO-66 in the electrospun scaffolds, the PZ and PZ-2U electrospun scaffolds were analyzed using an FTIR spectrophotometer (6300, Jasco/Germany) in transmittance mode and the wavenumber range of 4000–350 $cm^{-1}$.

## XRD

The PZ and PZ-2U scaffolds' crystallinity was examined using XRD (D8ADVANCE, Bruker/Germany) $2\theta = 5–35°$ at room temperature. The apparatus had a position-sensitive detector (Cu Kα radiation ($\lambda$) = 0.15406 nm), and the analysis voltage, time, and step sizes were set to 40 kV, 1.5 s, and 0.5°, respectively.

## Surface Hydrophilicity Evaluation

Given its substantial impact on cell adhesion, proliferation, and development, contact angle measurement was performed to assess the hydrophilicity of all the scaffolds utilizing a contact angle meter (XCA-50/Iran). For this purpose, a drop of 4 µl of distilled water was applied to the samples' surface in three distinct locations using a micro syringe at room temperature. The contact angles were then recorded after 30 s.

## Mechanical Analyses

A uniaxial tensile machine (ZwickRoell, Germany) based on ASTM D882 was used to investigate the tensile behavior of all the fabricated scaffolds at room temperature. For each group, a minimum of three samples were cut to 30 mm in length and 5 mm in width, and their thickness was carefully measured by a micrometer. The scaffolds were then clamped between the 20 mm-spacing jaws of the apparatus and stretched until sample failure was achieved using a load cell of 20 N and a tension rate of 2 mm/min. Ultimate tensile strength, elongation at break, and Young's modulus were reported as results of this characterization.

## Thermal Characterizations

### Thermogravimetric Analysis (TGA)

Based on the ASTM E1131, TGA (Mettler Toledo/USA) was employed to assess the thermal behavior of the PZ and PZ-2U scaffolds and validate the quantity of the UiO-66 present in the composite scaffold. The electrospun scaffolds, which weighed approximately 2 mg, were heated in a nitrogen environment at a flow rate of 50 ml/min, between 25 and 590 °C, at a rate of 10 °C/min.

### Differential Scanning Calorimetry (DSC)

The melting and crystallization properties of the PZ and PZ-2U electrospun scaffolds were measured using DSC (NETZSCH DSC 214 Polyma/Germany) in accordance with ASTM D3418. The samples with a mass of around 1 mg were put in aluminum pans and heated from 25 °C to 500 °C at a rate of 10 °C/min while being subjected to a nitrogen flow rate of 50 ml/min. The crystallization degree ($\chi_c$) was calculated using Eq. (2), in which $\Delta H_m$, $\phi_{PHB}$, and $\Delta H^0{}_m$ are representative of melting enthalpy, mass fraction of PHB in the sample, and melting enthalpy of 100% crystalline PHB that is equal to 146.6 J/g, respectively [7]. Also, the melting enthalpy can be calculated by measuring the area under the first peak in DSC plots.

$$\chi_c = \frac{\Delta H_m/\Phi_{PHB}}{\Delta H_m^0} \tag{2}$$

## In vitro Degradation

ASTM F1635 was followed in the biodegradation assessment of the PZ and PZ-2U electrospun scaffolds. Following cutting and weighing the materials into 1 × 1 $cm^2$ pieces, they were submerged in PBS solution at 37 °C for a duration of 100 days. For every interval period, following three rinses in distilled water and 4 h of vacuum drying at 37 °C, the weight loss of each sample was determined using Eq. (3):

$$\text{Weight loss } (\%) = \frac{W_0 - W_t}{W_0} \times 100\% \tag{3}$$

In Eq. (3), $W_0$ and $W_t$ represent the initial and sample weights at each time interval, respectively, which are measured using a scale with an accuracy of 0.00001 g. Following the final day of the degradation analysis, FTIR and SEM examinations were performed on the PZ-2U scaffold to search for morphological and chemical changes resulting from the degradation process.

## Bioactivity Assessment

Kokubo and Takadama's [42] protocol was followed while assessing the bioactivity of the PZ and PZ-2U scaffolds. The scaffolds, measuring 1 × 1 $cm^2$ and having a thickness of 0.03 to 0.04 mm, were submerged for 28 days at 37 °C in 15 ml of SBF solution. After day 28 of immersion in SBF, SEM (LEO 1430 VP/Germany), EDS (EDAX Element Silicon Drift Detector, Apolo), and XRD (D8ADVANCE, Bruker/Germany) analyses were utilized to detect and investigate the chemical composition and crystalline structure of the absorbed hydroxyapatite crystals on the surface of scaffolds.

## Cellular Behavior Evaluations

Cell culture experiments were performed to assess the behavior of MG-63 cells in response to the PZ and PZ-2U scaffolds. MG-63 cells were cultured in DMEM containing 10% FBS, 1% penicillin-streptomycin, and 1% L-glutamine and then incubated at 37 °C with 5% $CO_2$. Prior to preparation, the electrospun scaffolds were initially trimmed into circular sheets of 0.5, 1, and 2 $cm^2$ in diameter. Next, the scaffolds were sterilized by submerging them in ethanol for a duration of 10 min, repeating the process three times. In order to completely sterilize the scaffolds, they were additionally exposed to UV radiation for 30 min. Then, the scaffolds were washed three times with sterile PBS. Upon reaching 80% confluence, the MG-63 cells were harvested using trypsin-EDTA. MG-63 cells were placed on each scaffold by depositing the cell suspension and incubated for 30 min in an incubator (IN 22, Memmert/Germany) at a temperature of 37 °C with a $CO_2$ concentration of 5%. Subsequently, a volume of 1 ml of culture media was introduced into every well. The culture medium was periodically refreshed every other day. The well without scaffolding was considered as the control group in the following tests.

### Cell Viability

The MTT test was used to determine the cell viability based on ISO-10993-5. After the 1st, 3rd, and 7th days of cell seeding at a density of $3 \times 10^3$ cells/cm$^2$, 40 µl of MTT solution was applied to the cells, and they were then incubated for 4 h at 37 °C with 5% $CO_2$. Following the addition of 400 µl of DMSO solution to each sample's suspension, the formazan crystals were dissolved. Eventually, an ELISA plate reader (680, Bio-Rad, Hercules, CA/USA) was used to detect the absorbance of each sample at the wavelength of 570 nm.

### Cell Attachment

The experiment involved inserting sterilized scaffolds into 24-well plates and culturing them with MG-63 cells at a density of $3 \times 10^3$ cells/cm$^2$ to evaluate their adhesion and growth. After the 1st and 7th days, the scaffolds were soaked in PBS three times, and then the cells were fixed using a solution containing 2.5% glutaraldehyde in PBS. Subsequently, the scaffolds were kept at 4 °C for 1 h and then dehydrated using graded ethanol solutions at 30, 70, 90, 96, and 100 v/v%, with 10 min on each step. The dried scaffolds were then coated in gold (BalTec SCD005 machine), and the cell morphology of the cultured samples was examined utilizing an SEM (LEO 1430 VP/Germany).

### DAPI Staining

After seeding cells on scaffolds at a density of $3 \times 10^3$ cells/cm$^2$, the samples were allowed to incubate for 1 and 7 days. Subsequently, the culture fluids were washed with PBS. After being fixed using a 4% paraformaldehyde phosphate solution and stored in a refrigerator for 1 h, the samples were washed with PBS and stained with DAPI reagent. Stained cells on the scaffold were then imaged using a fluorescence microscope (Leica, Germany).

### ALP Activity

Phosphate is separated from p-nitrophenyl phosphate and transformed into p-nitrophenol by the ALP enzyme produced by osteoblast cells. These p-nitrophenols' light absorbance serves as a biochemical signal for assessing the osteoblast activity of the scaffolds grown in cell culture [7]. MG-63 cells were seeded on the scaffolds at a density of $3 \times 10^3$ cells/cm$^2$ and the ALP activity was evaluated on the 7th and 14th days of cultivation in accordance with the manufacturer's instructions for the ALP kit (Darman-Kave/Iran).

### Alizarin Red Staining

The alizarin red staining assay was carried out to evaluate the capacity of MG-63 cells cultured on the scaffolds to produce calcium phosphate and deposit it into a mineralized matrix. Cells were seeded on the scaffolds in a 24-well plate at a density of $3 \times 10^3$ cells/cm$^2$. After days 7 and 14, the cells were washed twice with PBS and then fixed for 30 min at room temperature with 4% paraformaldehyde. Afterward, the samples were treated with 0.5 ml of alizarin red staining solution (pH=4.1–4.3) for 30 min at room temperature after being twice rinsed with distilled water. Finally, once the surplus dye was removed by washing the samples five times with distilled water, they were digitally scanned (SCC 101P, Samsung/Korea).

### Quantitive Real-time Polymerase Chain Reaction (qRT-PCR) Assay

For 7, 14, and 21 days, the MG-63 cells were cultured at a density of $3 \times 10^3$ cells/cm$^2$ onto the scaffolds. The quantity of runt-related transcription factor 2 (RUNX2), osteocalcin (OCN), and collagen type 1 (COLI) gene expression, as the indicators linked with bone, was assessed using qRT-PCR to evaluate the scaffolds' potential to induce bone formation. Total RNA was extracted using an RNA extraction kit, and then a NanoDrop spectrophotometer (BioTek Epoch, USA) was utilized to measure the RNA concentration. Employing the iScript cDNA synthesis kit and the manufacturer's instructions, the RNA was reverse-transcribed into cDNA. Following completion of all necessary preparations, Applied Biosystems RT-PCR Instruments (Life Technologies, USA) were used to conduct the assays. The following conditions were followed for the PCR amplification: a 10-min incubation period at 95 °C and 40 cycles at 10-s intervals at 95 °C and 60 °C. In order to compare gene expression in different groups, the $2^{-\Delta\Delta Ct}$ technique was utilized, with β-actin serving as the reference gene. The qRT-PCR primers were designed and synthesized by Metabion (Germany) using the Gene Runner 6.0 program. Table 2 presents nucleotide sequences of primers used in this work.

## Statistical Analyses

Each test was conducted in a minimum of three duplicates, and the outcomes were expressed as the average ± standard

**Table 2** The nucleotide sequences of primers used for qRT-PCR assay

| Target genes | Primer sequences (F = forward, *R* = reverse) |
|---|---|
| RUNX2 | F: AACCCAGAAGGCACAGACAG<br>R: TTGGTGCAGAGTTCAGGGAG |
| OCN | F: ATGAGAGCCCTCACACTCC<br>R: TGGACACAAAGGCTGCAC |
| COLI | F: CCTCGGAGGAAACTTTGC<br>R: CTTCCCCATCATCTCCATTC |
| β-actin | F: TTCGAGCAAGAGATGGCCA<br>R: CACAGGACTCCATGCCCAG |

deviation. Statistical analyses were performed using Graph Pad Prism 9 (La Jolla, CA, USA). The one-way ANOVA analysis was used to ascertain statistical differences in the data with a significance level of $p < 0.05$.

## Results and Discussion

### Characterization of the Synthesized UiO-66 MOF

Figure 1(A) illustrates the FT-IR spectra of UiO-66. The broad peak at 3386 cm$^{-1}$ corresponds to the presence of OH groups due to intercrystalline water and physisorbed water condensed inside the cavities [43, 44]. The peak related to the aromatic C-H modes of the aromatic ring in the BDC linker is located at 2930 cm$^{-1}$ [45]. The most prominent characteristic peaks positioned at 1410 and 1595 cm$^{-1}$ are allocated to symmetric and asymmetric stretching of the carboxylate group (O-C-O) of the BDC linker, respectively. Furthermore, the weak band observed at 1508 cm$^{-1}$ is assigned to C=C vibrations benzene rings. The peaks around 650–1170 cm$^{-1}$ can be ascribed to the ZrO single bond stretching vibration [43, 46–48]. At lower frequencies, OH and CH vibrations of the BDC ligand overlapped with ZrO modes [49]. Also, The vibration modes at 661 and 470 cm$^{-1}$ can be attributed to $\mu_3$-O stretch and $\mu_3$-OH stretch in the UiO-66 framework, respectively. Moreover, the absence of any peak at 1658 cm$^{-1}$ can confirm the complete removal of DMF [43, 50].

The synthesized particles' crystalline structure was examined using XRD. Figure 1(B) shows the XRD pattern of the as-synthesized UiO-66. The sharp peaks with narrow distribution indicate the particles' high degree of crystallinity [44]. All of the characteristic diffraction peaks are in good agreement with the database's simulated result (PDF-Number: 96-413-2640) [51]. Six major characteristic peaks at 2θ = 7.4°, 8.6°, 14.8°, 17.2°, 25.8°, and 30.8° are attributed to the (111), (002), (222), (004), (006), and (117) planes of UiO-66, respectively. Furthermore, some minor peaks located at 2θ = 12.1°, 14.2°, 18.7°, 19.2°, 21.0°, 22.3°, 24.3°, 25.5°, 28.3°, 29.9°, 30.8°, 32.3°, 33.2°, and 34.6°corresponding to (022), (113), (133), (024), (224), (115), (044), (135), (335), (444), (117), (246), (355), and (008) diffraction planes, respectively, closely match the literature [43, 52]. Furthermore, a symmetry-forbidden low-angle reflection at around 2θ = 6° can be due to the presence of defects within the structure of UiO-66 [53, 54].

The morphology of the synthesized UiO-66 particles observed by FESEM and TEM is demonstrated in Fig. 2(A, B). According to the FESEM result, the octahedral UiO-66 crystals have a particle size distribution ranging from 80 to 200 nm. Moreover, based on the TEM images displayed in Fig. 2(C, D), the octahedral morphology of as-synthesized UiO-66 crystals was verified, and the identical particle size

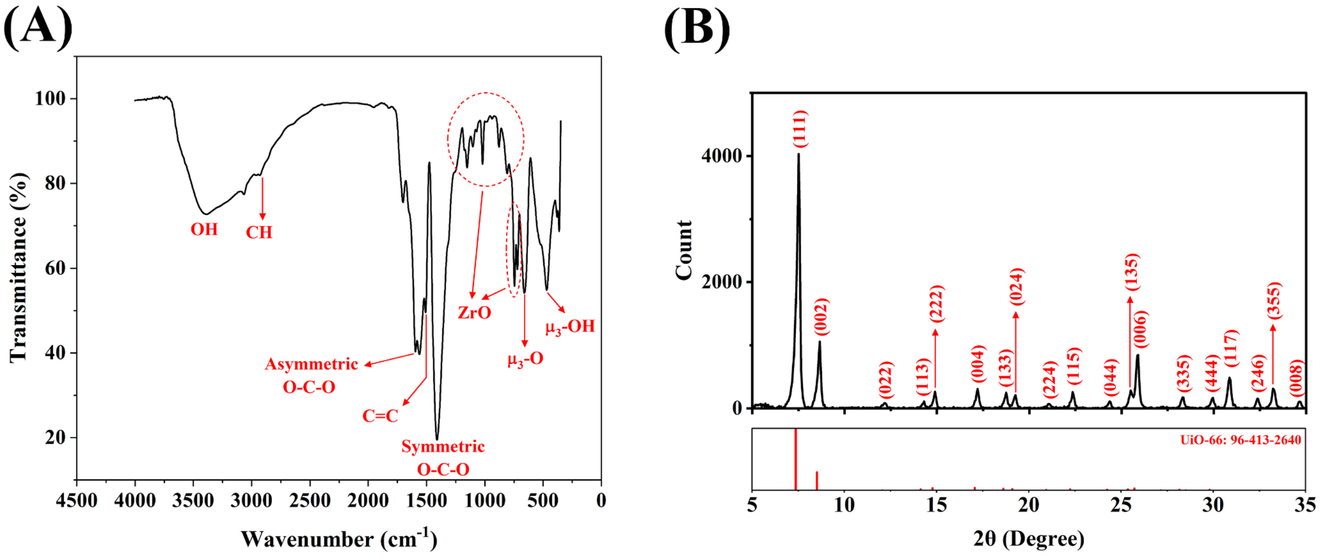

**Fig. 1** (A) FTIR and (B) XRD spectra of the synthesized UiO-66

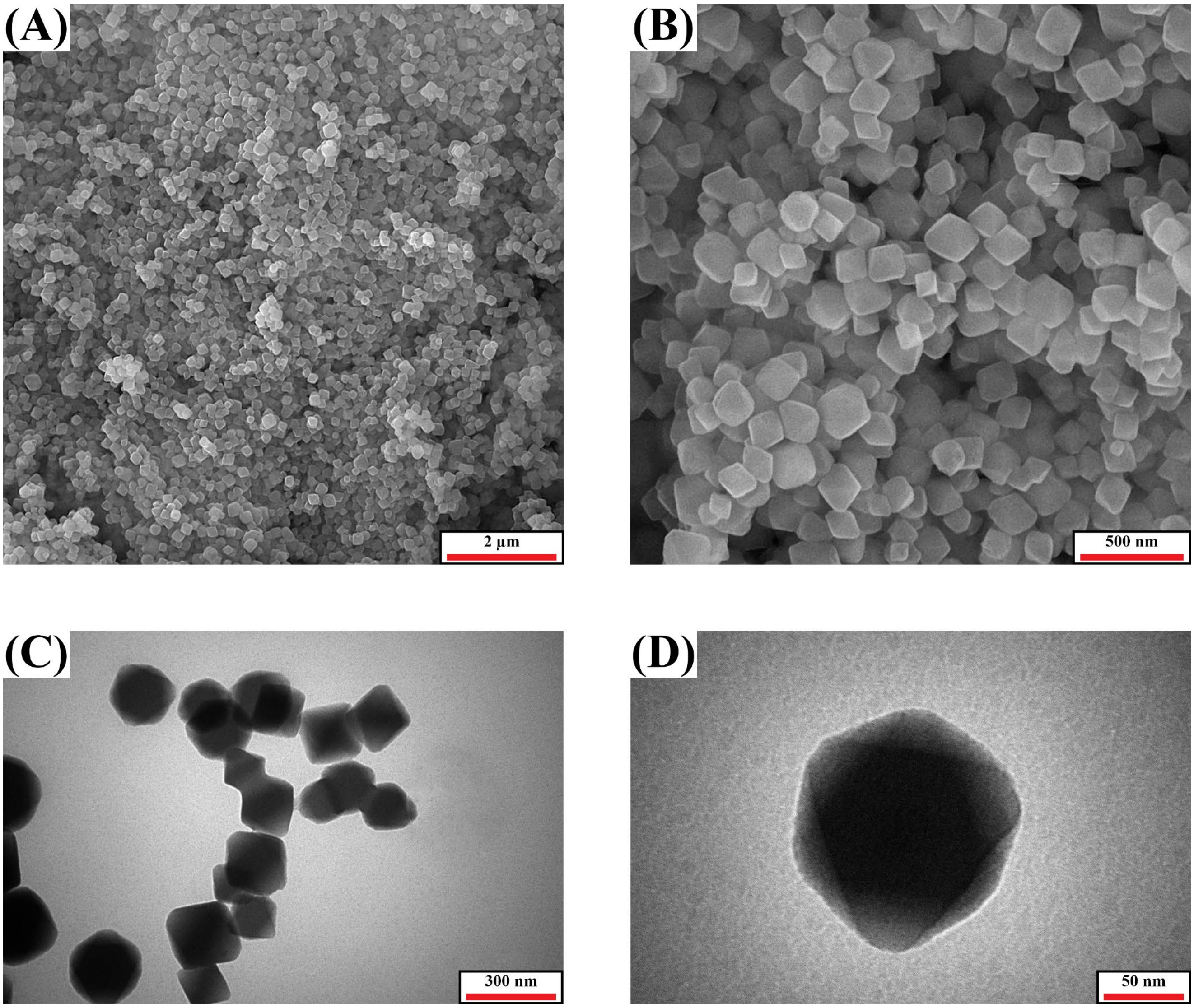

**Fig. 2** (A), (B) FESEM and (C), (D) TEM images of the synthesized UiO-66

in comparison with the one calculated using FESEM images was achieved.

According to the FTIR, XRD, FESEM, and TEM results, the successful synthesis of the UiO-66 particles was confirmed.

## Evaluation of the Fabricated Scaffold's Morphology

### SEM Imaging

The morphology of the electrospun scaffolds, determined by fiber diameter distribution, porosity percentage, and uniformity of the fibers, is a critical factor that affects cell behavior [7]. Figure 3 demonstrates the SEM images of the fabricated scaffold at three different magnifications, along with the histograms of the fiber diameters. As shown, all samples are entirely porous, homogeneous, and bead-free. Also, the average fiber diameter and porosity percentage at three layers of the prepared samples are illustrated in Fig. 4. Regarding the results in Fig. 4(A), the addition of 0.5 wt% of UiO-66 particles to the PZ scaffold has significantly reduced fiber diameter from 422 ± 90 nm to 347 ± 48 nm ($p < 0.05$). As the pH value of the solution falls below 8.3, due to the Zr–OH on the Zr node's tendency to form Zr–$OH_2^+$, UiO-66 is positively charged [55]. Subsequently, the charge production would result in increasing the conductivity and more fiber stretch in the magnetic field, and finally, fiber diameter reduction. Fu et al. [56] and Ahmadijokani et al. [57] also reported a decrease in fiber diameter as a result of UiO-66 incorporation into the poly(vinylidene fluoride) and chitosan/polyvinyl alcohol electrospun fibers, respectively. As demonstrated, increasing the amount of UiO-66

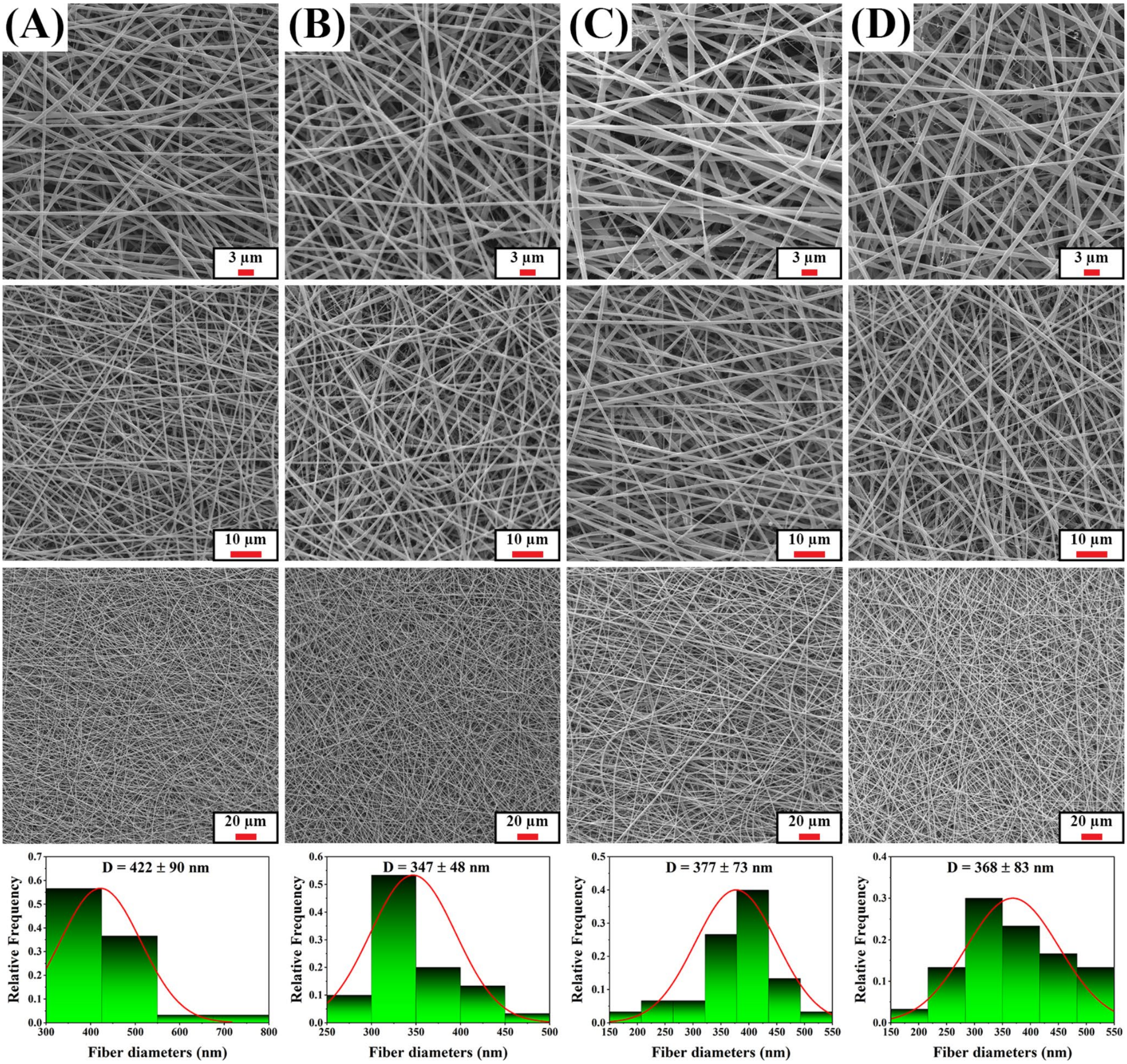

**Fig. 3** SEM images at different magnifications and fiber diameter histograms of the fabricated electrospun scaffolds of (A) PZ, (B) PZ-0.5U, (C) PZ-1U, and (D) PZ-2U

up to 2 wt% in the composite scaffolds had no significant change in fiber diameter ($p > 0.05$). By incrementing the amount of UiO-66, the solution's viscosity will increase, leading to the increment of fiber diameter. So, by adding more UiO-66 particles, the viscosity increment's adverse effect would counteract the conductivity increase and halt the further reduction of fiber diameter. Likewise, according to the results, adding UiO-66 particles causes the production of more uniform fibers with less standard deviation in comparison with the PZ sample.

In addition, porosity is regarded as another fundamental parameter for the morphology assessment of scaffolds used in tissue engineering. Not only is the porosity of the scaffolds, but also the interconnectivity of their pores is a critical issue to ensuring cellular migration and growth, nutrition supply, transferring signaling molecules, and removal of metabolic wastes [19, 58]. Based on the literature, porosity percentages above 80%, 40%, and 20% in the first, second, and third layers of scaffolds, respectively, are required to achieve interconnectivity and appropriate cell response [15]. As exhibited in Fig. 4(B), all of the fabricated scaffolds showed proper porosity in different layers, and UiO-66 incorporation had no unfavorable effect on the porosity of the composite scaffolds.

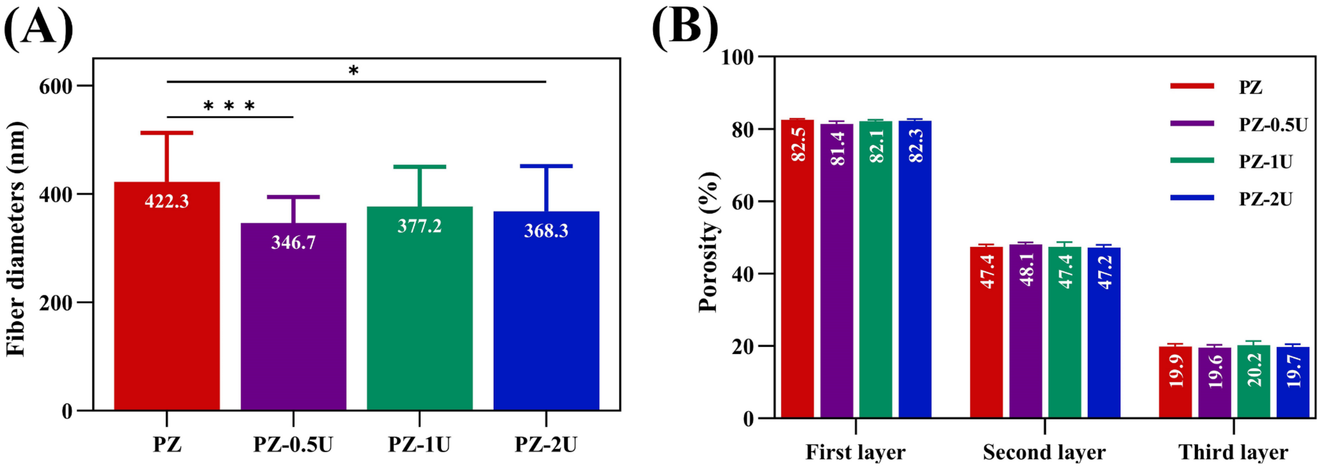

**Fig. 4** (A) The average fiber diameters, and (B) the porosity percentage in three layers calculated by MATLAB (R2019) of the fabricated electrospun scaffolds (*$p<0.05$, *** $p<0.001$)

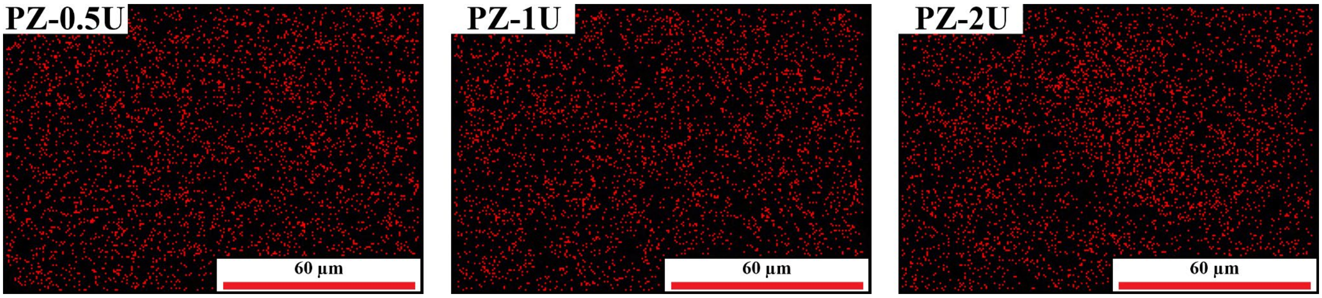

**Fig. 5** Distribution of Zr chemical element in the fabricated electrospun composite scaffolds captured using EDS mapping

### EDS Mapping

The composite scaffolds' mechanical, chemical, and biological characteristics depend on the uniform dispersion of the ceramic phase within the polymeric matrix [23]. In Fig. 5, in which EDS mapping related to composite scaffolds was shown, the red dots demonstrate Zr chemical element distribution in the fabricated electrospun scaffolds. As illustrated, the homogeneous dispersion of the UiO-66 particles and lack of agglomeration in fibers of all composite samples is evident, which can verify the suitable dispersion of UiO-66 particles during solution preparation.

### TEM

To assess the presence and distribution of the UiO-66 particles within the electrospun fibers, the TEM images at different magnifications of the PZ-2U electrospun composite scaffold were captured and exhibited in Fig. 6. As highlighted by red circles, the UiO-66 particles are evenly embedded in the polymer matrix, and the presence of no particle agglomeration is detected. The homogenous scattering of UiO-66 particles signifies good compatibility between the MOF phase and polymeric matrix [34]. In addition, as portrayed, in some parts of the composite fibers, the UiO-66 particles came to the edge of the surface, which is effective in increasing the surface roughness. However, for more accurate evaluations, the AFM analysis should be carried out. Moreover, it is worthwhile to mention that the size of UiO-66 particles is consistent with the size previously measured through FESEM and TEM images in MOF characterization.

### AFM

In order to evaluate the effect of UiO-66 addition on surface roughness, the AFM assessment on the PZ and PZ-2U scaffold was executed, and the results are demonstrated in Fig. 7. Regarding the outputs, upon the incorporation of the UiO-66 in the electrospun composite scaffold, both the average surface roughness (Ra) and the root mean square roughness (Rq) increased from 282.2 ± 52 nm to 332.7 ± 73 nm and from 353.7 ± 78 nm to 418.5 ± 84 nm, respectively. The findings indicate that the UiO-66 incorporation can considerably enhance the surface roughness. Wang et al. [34] demonstrated that the addition of UiO-66-$NH_2$ (a modified version of UiO-66 with a similar structure) to the chitosan membrane had a similar output and increased the surface

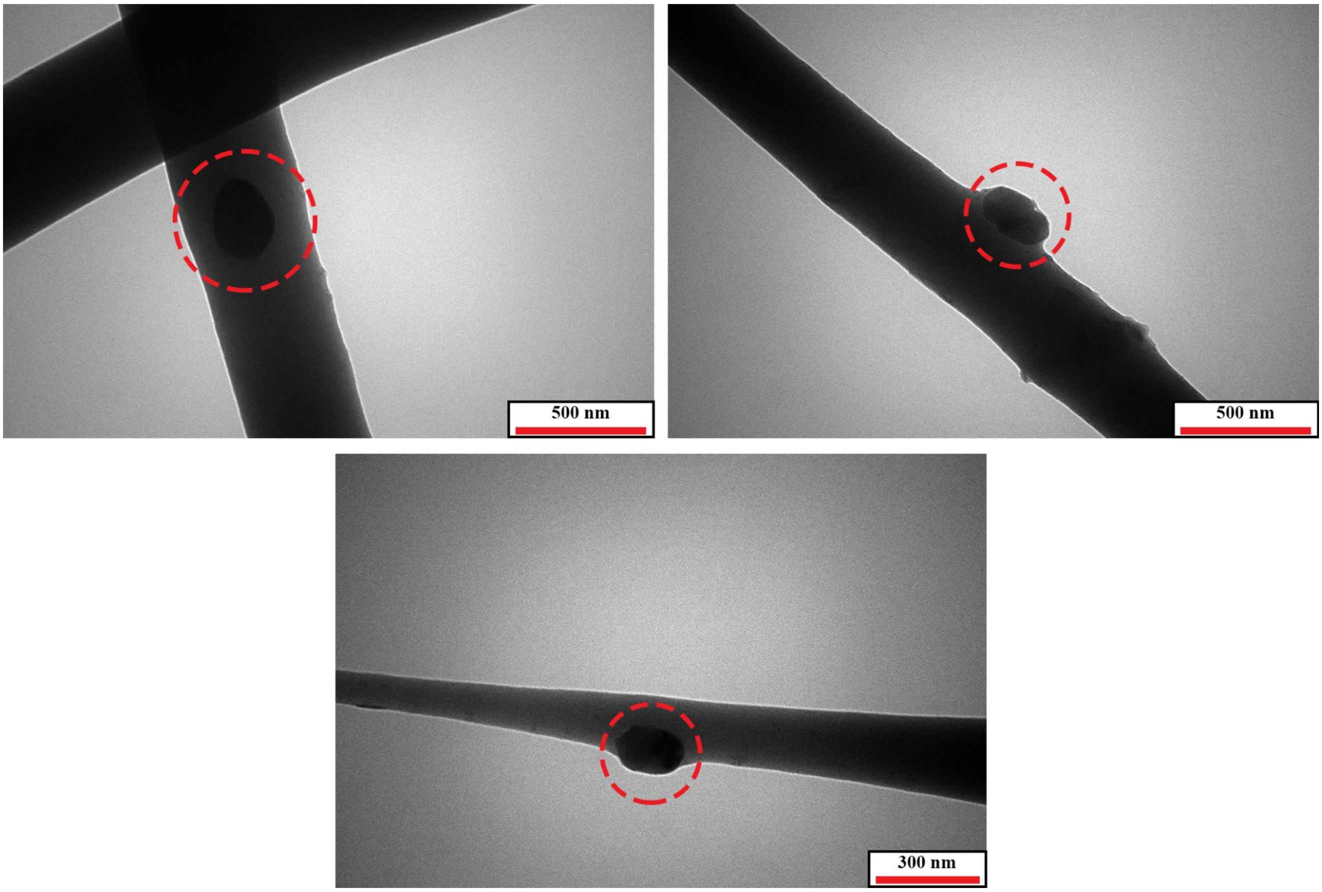

**Fig. 6** TEM images of the PZ-2U electrospun composite scaffold. (The circles indicate the presence of UiO-66 particles in the fibers)

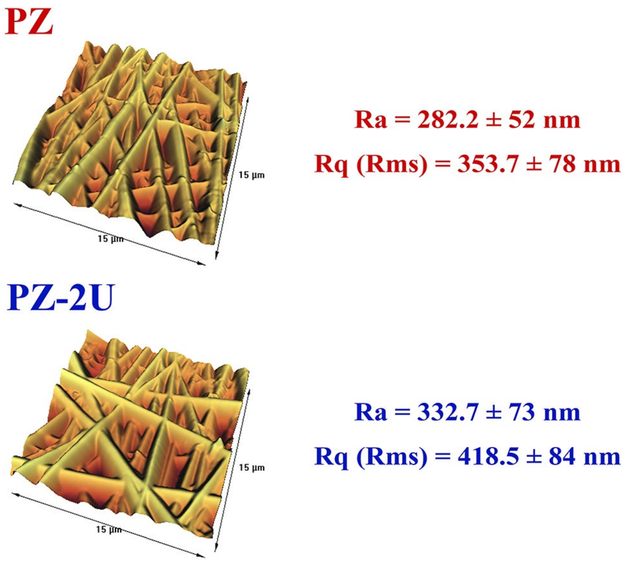

**Fig. 7** AFM 3D images of the PZ and PZ-2U electrospun scaffolds

roughness. Also, the AFM results are consistent with the findings of TEM images of the electrospun composite scaffold, which showed the influential effect of the UiO-66 on surface roughness enhancement. According to the literature, enhanced roughness of the biomaterial surface can benefit the osteoblast's initial attachment, proliferation, and differentiation [59, 60].

## FTIR

The FTIR spectra of the PZ and PZ-2U electrospun composite scaffolds are displayed in Fig. 8(A). Considering the characteristic peak at 1453 cm$^{-1}$ as the reference band [61], the absorbance values were normalized to make the comparison more logical and straightforward. A comprehensive analysis of the characteristic peaks of the synthesized UiO-66 was discussed in previous sections. Also, the FTIR spectrum of the PZ scaffold was thoroughly inspected during our previous work [7]. Briefly, the peaks at 3436 and 1730 cm$^{-1}$ are related to the hydroxyl and carbonyl groups of PHB, respectively. Moreover, the presence of zein in the PZ scaffold can be verified by the peaks at 3290, 1657, and 1543 cm$^{-1}$ corresponding to amide A, amide I, and amide II of zein, respectively. The peak observed at 1226 cm$^{-1}$ is associated with the overlap between amide III of zein and PHB's C-O-C group. It is worth mentioning, regarding the literature, that the distinctive peak at 3290 cm$^{-1}$ can be

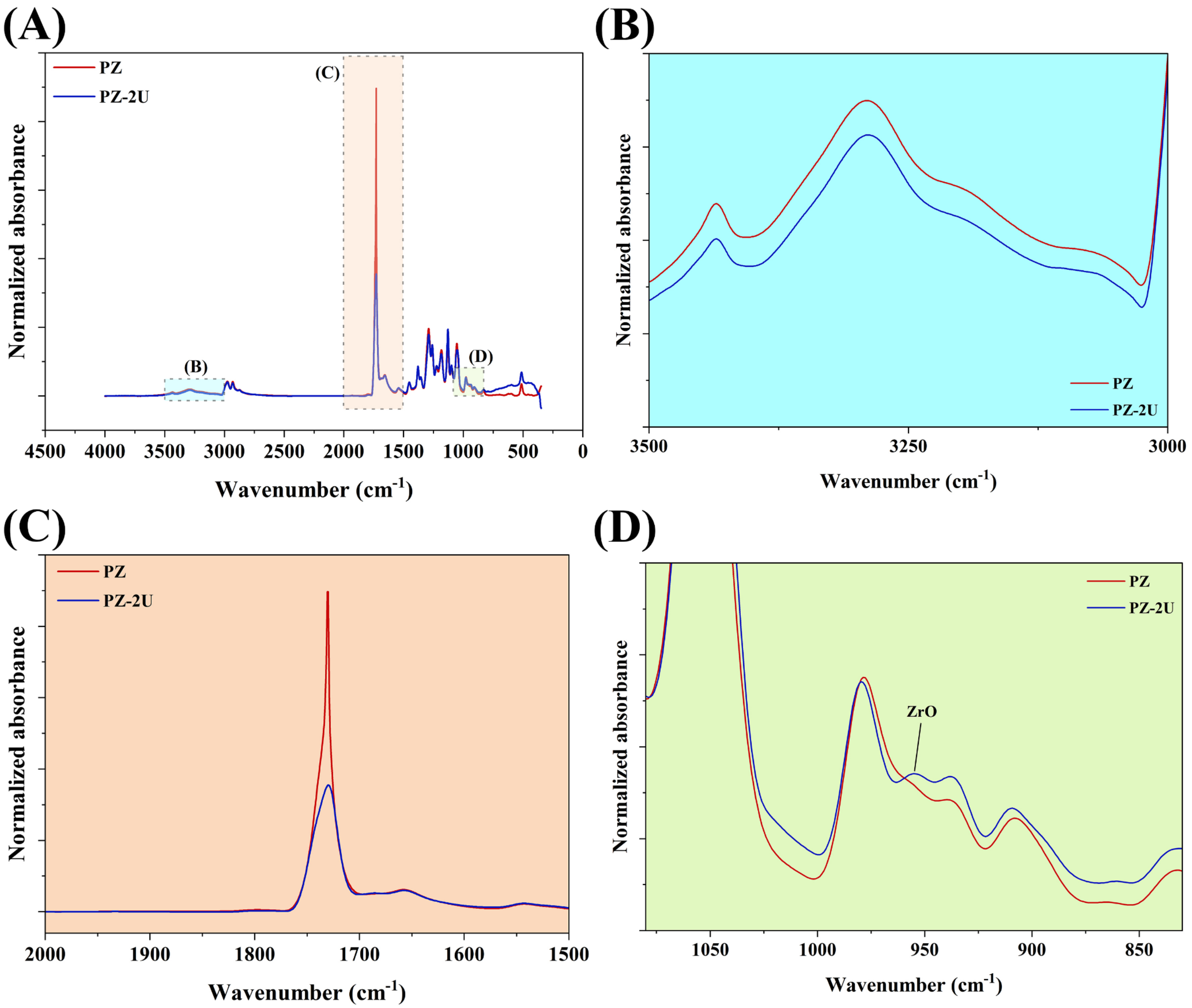

**Fig. 8** (A) FTIR spectra of the PZ and PZ-2U electrospun scaffolds, (B), (C), and (D) The enlarged sections of FTIR spectra of the PZ and PZ-2U electrospun scaffolds in specific wavenumber regions

attributed to the formation of a hydrogen bond between the amide groups in zein and the carbonyl group of PHB [7].

After adding UiO-66 to the PZ scaffold, the peak at 3290 $cm^{-1}$, enlarged in Fig. 8(B) and indicates a hydrogen bond between PHB and zein, has become broader and less intense. This change suggests the interactions between UiO-66 crystals with PHB and zein polymers through hydrogen bonding, reducing the intensity of the peak related to the previously formed hydrogen bond in the PZ scaffold chemical structure [62]. Likewise, as depicted in Fig. 8(C), the peak at 1730 $cm^{-1}$, related to the carbonyl groups of PHB, has become less intense, possibly due to coordination bonds between $Zr^{4+}$ ions in UiO-66, which are accessible from missing linker defects, and the PHB's carbonyl groups. These bonds can consume free carbonyl groups in PHB, leading to a less intense peak. Another worth-noting change is the emergence of a new characteristic peak at 955 $cm^{-1}$, enlarged in Fig. 8(D), which can be attributed to the ZrO single bond stretching vibration in UiO-66. The absence of this peak in the PZ spectrum can prove the presence of UiO-66 in the chemical structure of the PZ-2U electrospun composite scaffold. The lack of additional characteristic peaks of UiO-66 in the FTIR spectrum of the PZ-2U sample could be explained by the insensitivity of the FTIR technique and the small quantity of UiO-66 present in the fabricated scaffold's structure. In addition, UiO-66's vibrational bands may overlap with those of PHB and zein [21].

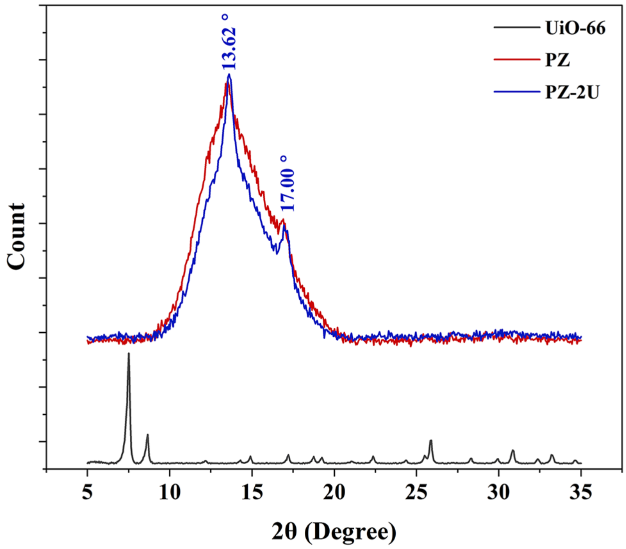

**Fig. 9** XRD pattern of UiO-66 powder along with the PZ and PZ-2U electrospun scaffolds

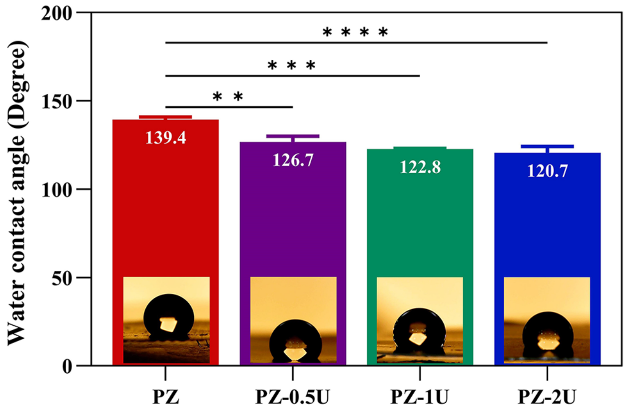

**Fig. 10** Water contact angle measurement of the electrospun scaffolds after 30 s (** $p<0.01$, *** $p<0.001$, **** $p<0.0001$)

## XRD

The XRD pattern of the UiO-66 crystals and the PZ and PZ-2U scaffolds is depicted in Fig. 9. The sharp and narrow characteristic peaks of UiO-66 were audited in previous sections. The diffraction pattern of the PZ scaffold exhibited two characteristic peaks at $2\theta=13.51°$ and $2\theta=16.83°$ assigned to the reflections of (020) and (110) planes, respectively, and are related to the α-form crystal modifications of PHB. In highly ordered PHB polymer, this form of crystals corresponds to an orthorhombic cell with the lattice parameters of a = 0.576 nm, b = 1.32 nm, and c = 0.599 nm, along with mutually perpendicular axes ($\alpha=\beta=\gamma=90°$) [7, 63]. However, no recognizable zein peaks were detected, known as two diffraction halos at 2θ values of 9.78° and 19.48°, which could be explained by the amorphous nature and low crystallinity percentage of this protein [7].

With the incorporation of UiO-66, the characteristic Bragg diffraction peaks of PHB at $2\theta=13.62°$ and $2\theta=17.00°$ in the PZ-2U composite scaffold experienced an increase in intensity, indicating the nucleation effect of UiO-66 could speed up PHB crystallization and eventually perfect the PHB crystallite [64]. It was expected that diffraction peaks of UiO-66 would be discerned in the XRD pattern of the PZ-2U scaffold. However, due to the small portion of UiO-66 within the composite, the peaks corresponding to the crystalline structure of UiO-66 could not be detected.

## Surface Hydrophilicity Evaluation

The results of water contact angle measurements of the electrospun scaffolds are depicted in Fig. 10. As illustrated, the addition of UiO-66 particles reduced the water contact angles significantly ($p<0.05$). However, the differences between groups containing UiO-66 were insignificant ($p>0.05$). Based on the results, incorporating 2 wt% UiO-66 increased the surface's hydrophilicity, leading to a decrease in the water contact angle from 139.4 ± 1.4° in the PZ scaffold to 120.7 ± 3.5° in the PZ-2U sample.

The non-defective UiO-66, whose $Zr_6$ cluster is surrounded by 12 organic linkers, exhibits hydrophobic behavior due to the hydrophobic nature of the phenyl rings. However, previous research has demonstrated that the presence of defects in the form of missing linkers in UiO-66 leads to opening Zr metal sites at the node, increasing Lewis-acid sites and turning them into hydrophilic [36, 44, 65]. Regarding the literature, lowering the synthesis temperature, using monovalent modulator molecules like hydrochloric acid and benzoic acid in the MOF synthesis reaction mixture, and reducing the BDC/Zr ratio are three techniques to induce defects in the structure of UiO-66 [53, 65]. Jajko et al. [53] showed that the lower the synthesis temperature, the greater the number of structural defects in the form of a missing linker. In their examinations, UiO-66 synthesized at 100 °C and 160 °C contained some defects, while the one that was synthesized at 200 °C revealed no defects. As mentioned in previous sections, in this research, the UiO-66 synthesis temperature was 120 °C, the BDC/Zr molar ratio was around one, and hydrochloric acid and benzoic acid were also utilized in the synthesis reaction mixture. Considering all of these conditions, as well as the XRD analysis of UiO-66, it is expected that the synthesized UiO-66 has a hydrophilic nature.

Karakecili et al. [38] also demonstrated that the scaffold containing chitosan and UiO-66 had an increased water uptake capacity with a higher percentage of UiO-66, attributed to the hydrophilic nature of UiO-66.

## Mechanical Analyses

The scaffolds designed for bone healing must have additional mechanical strength to support the various functions of each bone in the body, such as skeletal support, movement, and vital organ protection [32]. The mechanical analysis results, including stress-strain curves, as well as the values of Young's modulus (elastic modulus), ultimate tensile stress, and elongation at break, are presented in Fig. 11. It is evident that with the increase of UiO-66 particle percentage within the scaffolds structure, the values of Young's modulus and ultimate tensile stress increased significantly ($p<0.05$). According to the findings, the addition of 2 wt% UiO-66 MOF led to more than a 2-fold increase of Young's modulus, increasing from 100.9 ± 0.8 MPa for the PZ scaffold to 203.1 ± 0.2 MPa for the PZ-2U sample. Likewise, the ultimate tensile stress enhanced by approximately 90%, rising from 4.53 ± 0.41 MPa to 8.60 ± 0.99 MPa for the PZ and PZ-2U electrospun scaffolds, respectively. These substantial increases can be related to the coordination effect of $Zr^{4+}$ ions, caused by the UiO-66 defects, with the polymer matrix. The $Zr^{4+}$ ions are capable of forming coordination bonds with carbonyl groups on the PHB molecules, thereby strengthening the interaction between them [64]. In other words, the $Zr^{4+}$ ions function as bridges between the PHB chains, enhancing their interaction and ultimately leading to improved mechanical properties. Furthermore, it is reported that due to the abundant organic ligands present in the structure of MOFs, they are known to have excellent interface compatibility with polymers, distinguishing them from inorganic reinforcements. This compatibility allows them to act as a barrier, effectively preventing crack extension and dislocation movements rather than serving as stress concentration sites that absorb a significant amount of energy and encourage shear strain in the matrix [38, 66]. Moreover, research by Wu et al. [67] has demonstrated that UiO-66,

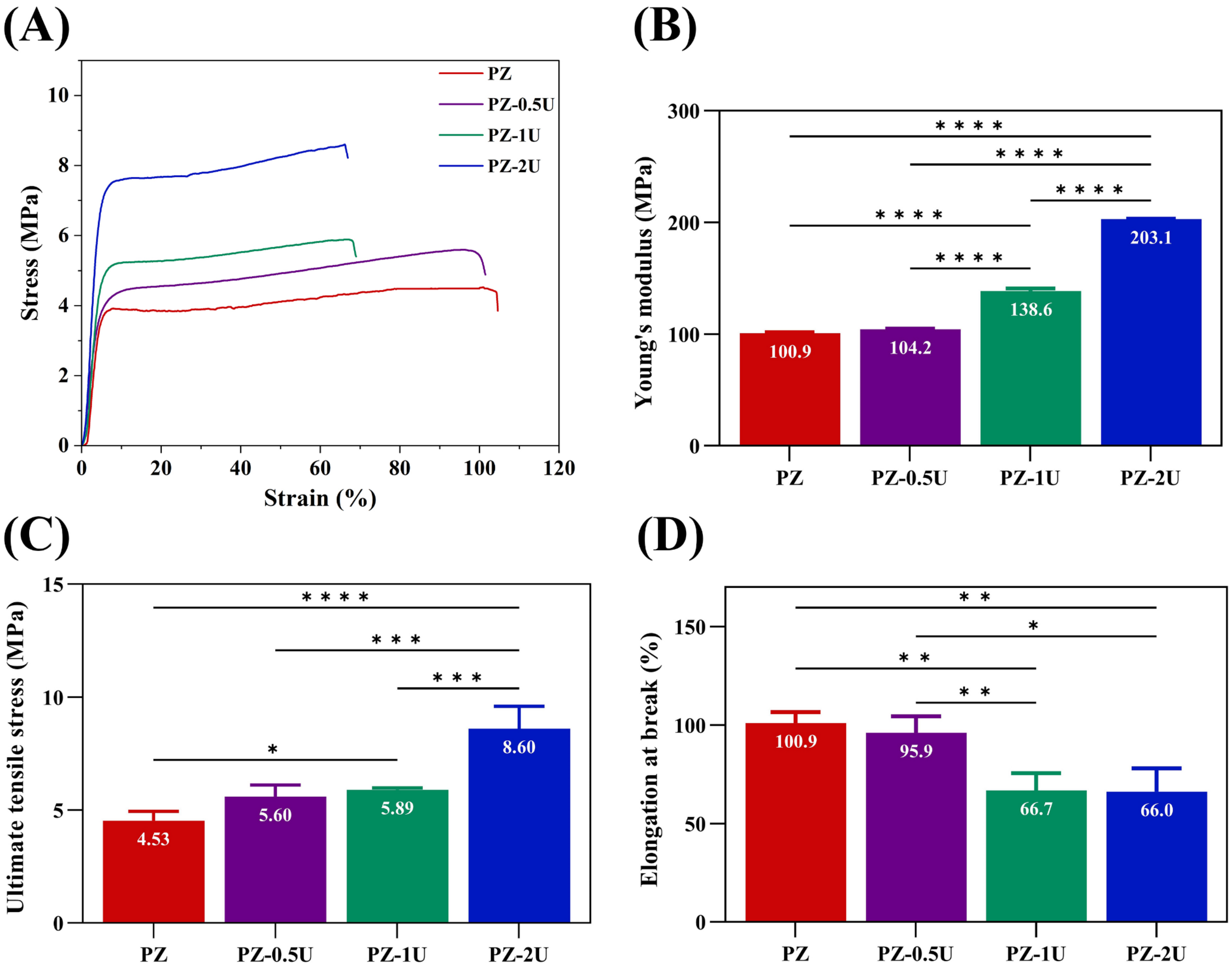

**Fig. 11** The tensile mechanical analyses of the fabricated electrospun scaffolds: (A) Stress-strain curves, (B) The values of Young's modulus, (C) The values of ultimate tensile stress, and (D) The values of elongation at break (*$p<0.05$, ** $p<0.01$, *** $p<0.001$, **** $p<0.0001$)

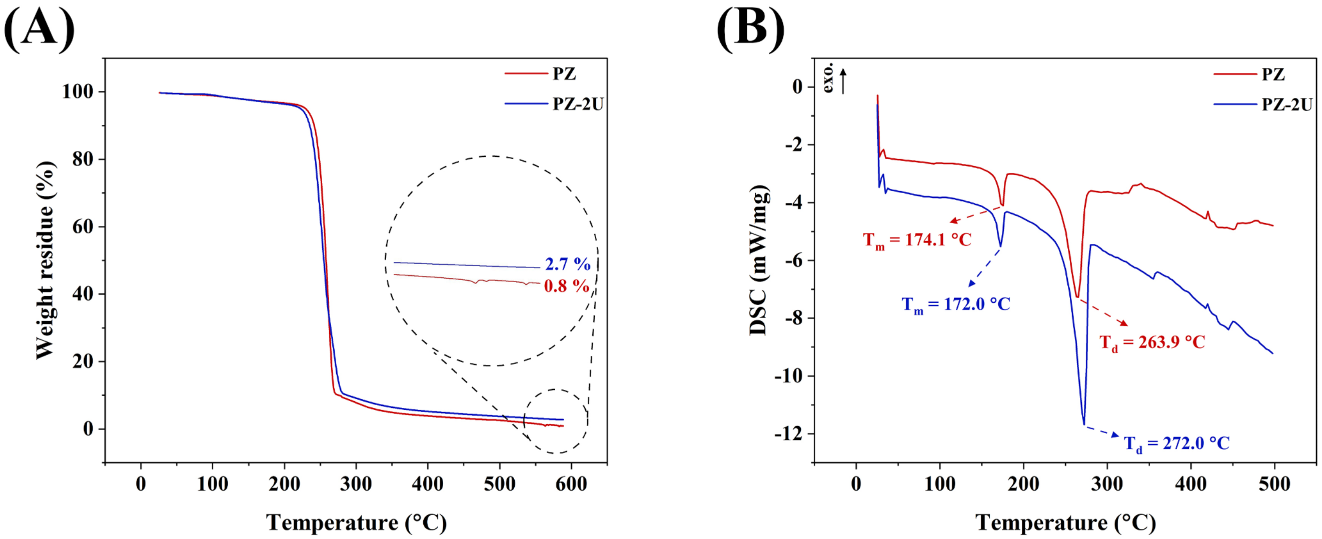

**Fig. 12** (A) TGA and (B) DSC curves of the PZ and PZ-2U electrospun scaffolds

**Table 3** Thermal points, melting enthalpy ($\Delta H_m$), and crystallization degree ($\chi_c$) of the PZ and PZ-2U electrospun scaffolds extracted from TGA and DSC figures

| Samples | $T_{d\,(5\%)}$ (°C) | $T_{d\,(10\%)}$ (°C) | $T_m$ (°C) | $T_d$ (°C) | $\Delta H_m$ (J/g) | $\chi_c$ (%) |
|---|---|---|---|---|---|---|
| PZ | 231.1 | 241.7 | 174.1 | 263.9 | 55.41 | 41.58 |
| PZ-2U | 224.6 | 235.6 | 172.0 | 272.0 | 57.73 | 44.18 |

despite its highly porous structure, possesses phenomenally high mechanical stability compared to other highly porous MOFs due to its high degree of coordination of Zr-O metal centers to the organic linkers. Also, the possible hydrogen bonding between UiO-66 and PHB and zein, as proved through FTIR analysis, can effectively enhance mechanical properties. In previous studies, Karakecili et al. [38], Yin et al. [64], and Lima et al. [68] reported improved mechanical properties after incorporating UiO-66 into chitosan scaffold, poly(ethylene terephthalate) film, and alginate hydrogel, respectively.

With regard to Fig. 11(D), the addition of UiO-66 to the scaffolds resulted in a significant decrease in the elongation at break values from 100.9 ± 5.6% for the PZ sample to 66.0 ± 12.0% for the PZ-2U scaffold ($p < 0.05$). Yin et al. [64], who also experienced the same trend after adding UiO-66 to poly(ethylene terephthalate) films, attributed this phenomenon to increased rigidity and brittleness of the composites resulting from coordination bonds between $Zr^{4+}$ ions of the defects in UiO-66 and the PHB's carbonyl groups. In addition, XRD examination revealed increased crystallinity in the composite scaffold after adding UiO-66, which will be confirmed through DSC assessment in the upcoming sections. The increased crystallinity might lead to increased brittleness and, consequently, reduced elongation at break.

Considering the literature, human cancellous bone, also called trabecular or spongy bone, generally possesses modulus and compressive strength ranging from 0.1 to 2 GPa and from 2 to 20 MPa, respectively, which verifies that the fabricated composite scaffold has sufficient mechanical properties for bone tissue engineering applications [69].

Due to its lower fiber diameter alongside improved hydrophilicity and mechanical properties, the PZ-2U sample was chosen as the optimum scaffold among the composite groups. Further examinations were performed on the PZ and PZ-2U scaffolds to investigate the effects of UiO-66 incorporation.

## Thermal Characterizations

### TGA

The TGA curves for the PZ and PZ-2U electrospun scaffolds are illustrated in Fig. 12(A). Additionally, the numerical findings, such as temperatures at which 5% and 10% weight loss occur ($T_{d\,(5\%)}$ and $T_{d\,(10\%)}$, respectively) are tabulated in Table 3. It is evident that both scaffolds underwent a single-stage thermal decomposition. The TGA of PZ-2U closely resembles that of PZ, indicating a low proportion of UiO-66 in the composite. According to the literature, the decomposition of UiO-66 MOF involves three distinct mass-loss stages. During the first stage, occurring below 100 °C, physisorbed water and the residual solvent trapped inside the porous structure of UiO-66 are released. Following that, the second stage, taking place between 100 and 450 °C, is associated with the removal of DMF and the dehydroxylation of the Zr oxo-clusters. Eventually, the last and most significant weight-loss stage starts at 450 °C and is attributed to the MOF structure decomposing into $ZrO_2$ residue, including thermal degradation of organic ligands and Zr clusters [47, 57, 70, 71]. Regarding the results presented in Fig. 12(A) and Table 3, it was observed that up to a temperature of 261 °C, the curve related to the PZ-2U sample is steeper than the PZ's. As a result, the $T_{d\ (5\%)}$ and $T_{d\ (10\%)}$ for the PZ-2U scaffold were slightly lower than those for the PZ sample. Similar observations were made in the works of Yin et al. [64], Aden et al. [47], and Shen et al. [70], indicating that polymer composites incorporating UiO-66 exhibited faster thermal degradation in certain parts of the TGA curves. Numerous investigations have shown that UiO-66 defects typically exist as missing linkers [72, 73]. This kind of defect leads $Zr^{4+}$ ions to be directly exposed to the polymer matrix. The exposed $Zr^{4+}$ may partially catalyze the degradation of the polymer matrix, resulting in a slight decrease in the initial decomposition temperatures [64]. Likewise, this phenomenon can also be justified by the initial stages of thermal decomposition of UiO-66, involving the loss of residual water and solvents, as well as the dehydroxylation of Zr oxo-clusters, leading to accelerated composite thermal decomposition up to a certain temperature threshold. However, after 261 °C, the slope of the PZ-2U diagram fell above the PZ sample. At this temperature, the UiO-66 framework still remains intact and can form a layer on the surface of the polymer melt, acting as a barrier for mass and heat transfer, thereby slowing down thermal degradation [70]. The final remaining weight of the samples showed approximately a 2% difference, confirming the proper dispersion of UiO-66 in the polymer matrix and supporting the claimed percentage of MOF in the composite scaffold structure. Although the residual weight of the composite (2.7%) was slightly more than the theoretical MOF content, this can be attributed to the high specific surface area of UiO-66 particles and their ability to entrap degraded products within their porous structure [18, 64].

### DSC

The melting behavior and crystallinity modifications of the scaffolds caused by the inclusion of the UiO-66 were investigated through the DSC technique. Figure 12(B) portrays the DCS results for the PZ and PZ-2U electrospun scaffolds. The data measured by DSC, including melting temperature ($T_m$), degradation temperature ($T_d$), melting enthalpy ($\Delta H_m$), and crystallization degree ($\chi_c$), is reported in Table 3. As can be seen, two endothermic peaks have been recorded in the DSC diagrams: $T_m$, where the as-formed crystals in electrospun fibers melt, and $T_d$, the temperature at which the scaffold structure decomposes. It is worthwhile to point out that since the glass transition temperature ($T_g$) of PHB is reported to be below 10 °C, it is not detectable in the figure presented [15]. Concerning the results, the $T_m$ value of the PZ scaffold has decreased from 174.1 °C to 172.0 °C after adding UiO-66 to fabricate the PZ-2U scaffold. This decrease was also observed by Yin et al. [64], who found a reduction in $T_m$ by increasing the UiO-66 content in poly(ethylene terephthalate). It may be attributed to the interaction between the MOF and the PHB, which can disrupt the polymer chains' folding and rearrangement, thereby lowering the melting point [64]. In addition to $T_m$, the crystallinity degree of the scaffolds can also be calculated using the area under the first endothermic peak in the DSC figure. As mentioned in Table 3, UiO-66 incorporation has increased the crystallinity degree from 41.58% for the PZ to 44.18% for the PZ-2U scaffold, which is consistent with XRD analysis outputs. This effect can be disclosed by the UiO-66's ability to act as a nucleating agent, promoting the formation of heterogeneous nucleation points and increasing crystallinity [64]. Furthermore, Ahmed et al. [74] revealed that increasing the percentage of UiO-66 in the poly(ethylene terephthalate)/UiO-66 composite encourages the crystallization of the polymer matrix.

The introduction of UiO-66 particles led to an increase in the $T_d$ from 263.9 °C to 272.2 °C in the PZ and PZ-2U scaffolds, respectively. As the polymer matrix melts, UiO-66 moves to the polymer surface, creating a robust diffusion barrier that acts as a shield, thus raising the activation energy for polymer degradation. Higher activation energy results in better thermal stability [70].

## In vitro Degradation

An ideal scaffold should degrade at a controlled rate, preferably matching the new bone tissue growth rate. If degradation occurs too slowly, it will not provide adequate structural support. On the other hand, if degradation happens too quickly, it can impede bone regeneration. The specific application should determine the rate at which the scaffolds degrade. For example, scaffolds used in spinal fusion procedures should last 9 months or longer, while those used in cranio-maxillofacial applications should last 3 to 6 months [75, 76]. Four processes are commonly involved in polymer degradation in aqueous environments: hydration, insufficient tensile strength, mass loss, and solubilization. In the following three sections, the in vitro degradation behavior of the PZ and PZ-2U scaffolds is evaluated through weight loss assessment, SEM images, and FTIR analysis.

### Weight Loss Evaluation

The curves of the remaining weight loss of the PZ and PZ-2U electrospun scaffolds over 100 days of immersion in PBS are plotted in Fig. 13(A). As illustrated, the PZ-2U scaffold started degrading at a faster rate from the first week, and after 100 days, 69.88% of the PZ scaffold and 57.40% of the PZ-2U scaffold remained. This higher in vitro degradation rate can result from enhanced hydrophilicity and less-diameter fibers, providing a higher surface-to-volume ratio [11]. Additionally, previous studies have shown that UiO-66 breaks down quickly in PBS at pH = 7.4. It has been observed that UiO-66, which is usually very stable in water, breaks down in PBS, possibly due to the production of zirconium oxide or the strong attraction of Zr atoms to phosphate groups [77].

### Morphology of the Fibers

The surface morphology of the PZ-2U fibers after being immersed in PBS at 37 °C for 100 days is demonstrated in Fig. 13(B). The two most common types of surface morphological changes in polymers during in vitro degradation are usually surface melting and fiber breaking. In contrast to the crystalline segments that fibers break during degradation, melting occurs in amorphous sections [7]. Our previous research [7] revealed that melting was the chief mode of degradation for the PZ scaffold due to the reduced crystallinity degree resulting from zein addition. However, as shown in Fig. 13(B), both fiber breakage and surface melting occurred during the degradation of the PZ-2U scaffold. This could be attributed to the increased crystallinity, as confirmed by XRD and DSC analyses, which resulted from the inclusion of UiO-66.

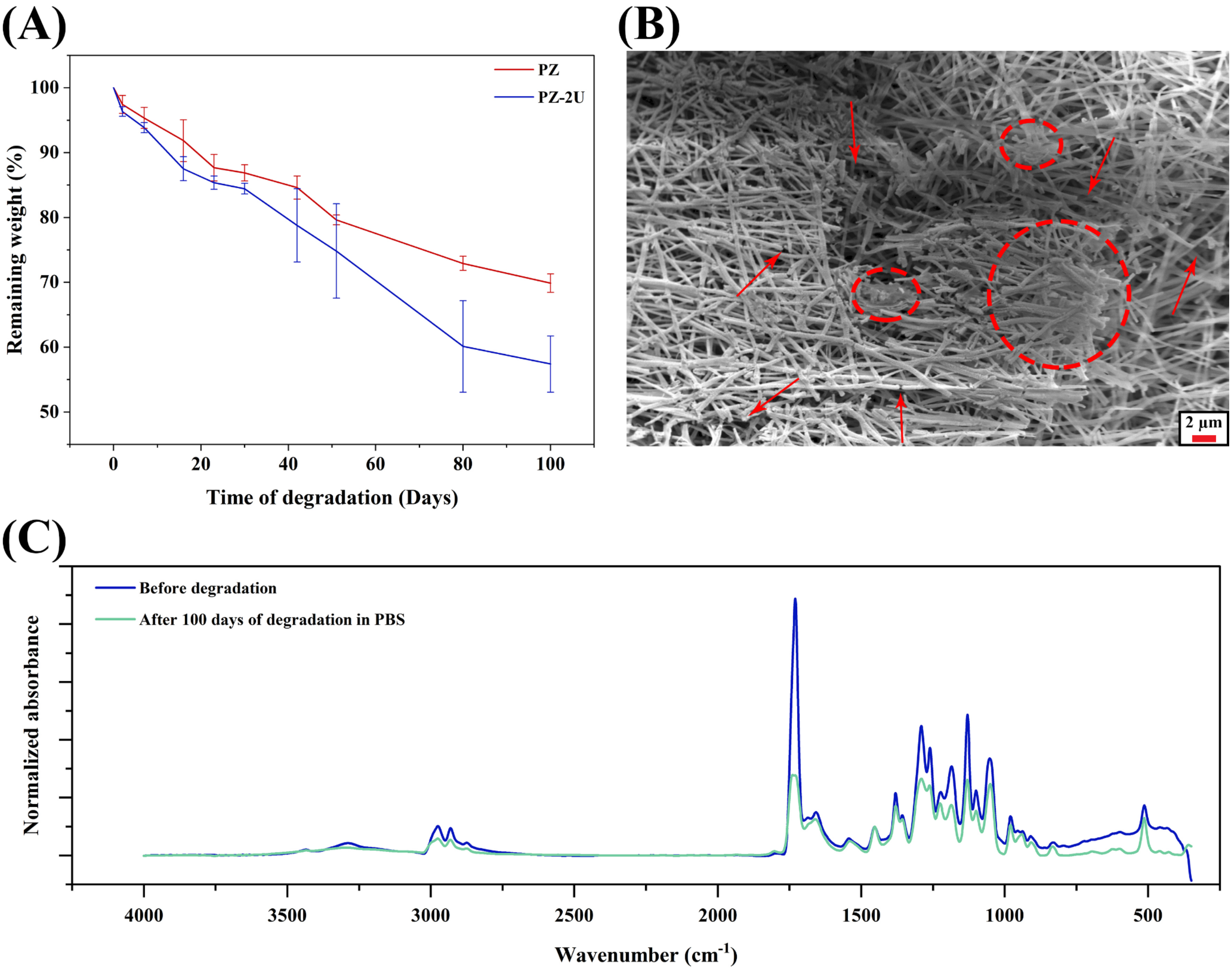

**Fig. 13** (A) The remaining weight percentage of the PZ and PZ-2U scaffolds over 100 days of degradation in PBS. (B) SEM image of the PZ-2U scaffold after 100 days of degradation in PBS (The arrows show fiber breakage, and the circles indicate surface melting). (C) FTIR spectra of the PZ-2U scaffold before and after 100 days of degradation in PBS

### FTIR Assessment

FTIR spectra of the PZ-2U after and before being degraded in PBS are normalized against the reference peak at 1453 cm$^{-1}$ and shown in Fig. 13(C). The peak at 3290 cm$^{-1}$, indicating hydrogen bonds between PHB, zein, and UiO-66, has been almost smoothed out, which can be related to the hydrolysis of these bonds. Likewise, other characteristic peaks have also experienced a remarkable reduction that can be explained by cleavage in the components and hydrolysis of the structure [78].

## Bioactivity Assessment

### Morphological Evaluation

SBF solution has an ion concentration that nearly resembles that of human blood. Consequently, the formation of apatite-like deposits on the surface of the scaffold following its immersion in SBF is a sign of its osteoconductive properties in the context of bone tissue engineering applications [15, 79]. In the process of biomineralization, this mineral layer provides physicochemical and mechanical cohesiveness between the scaffold and the natural bone [80]. The SEM images of the PZ and PZ-2U scaffolds after 28 days of immersion in SBF are illustrated in Fig. 14. It is clear that hydroxyapatite crystals formed on the surface of both scaffolds; however, larger and more uniform deposits were found on the PZ-2U's surface compared to the PZ's. This higher level of bioactivity may result from improved hydrophilicity and increased roughness due to the incorporation of UiO-66 [81]. Moreover, the phosphate anions ($PO_4^{3-}$) with negative charges can be attracted to the surface of the scaffolds due to the presence of $Zr^{4+}$ ions caused by defects in UiO-66, which will then lead to the adsorption of the calcium cations ($Ca^{2+}$). The development of calcium-phosphate nuclei is the ultimate result of these sequential and reversible interactions. These nuclei can undergo a phase change over time, eventually leading to the crystallization of the amorphous calcium-phosphate depositions, thus forming a stable layer of hydroxyapatite deposition on the surface. As a matter of fact, surfaces possessing higher bioactivity potential tend to be more capable of creating a

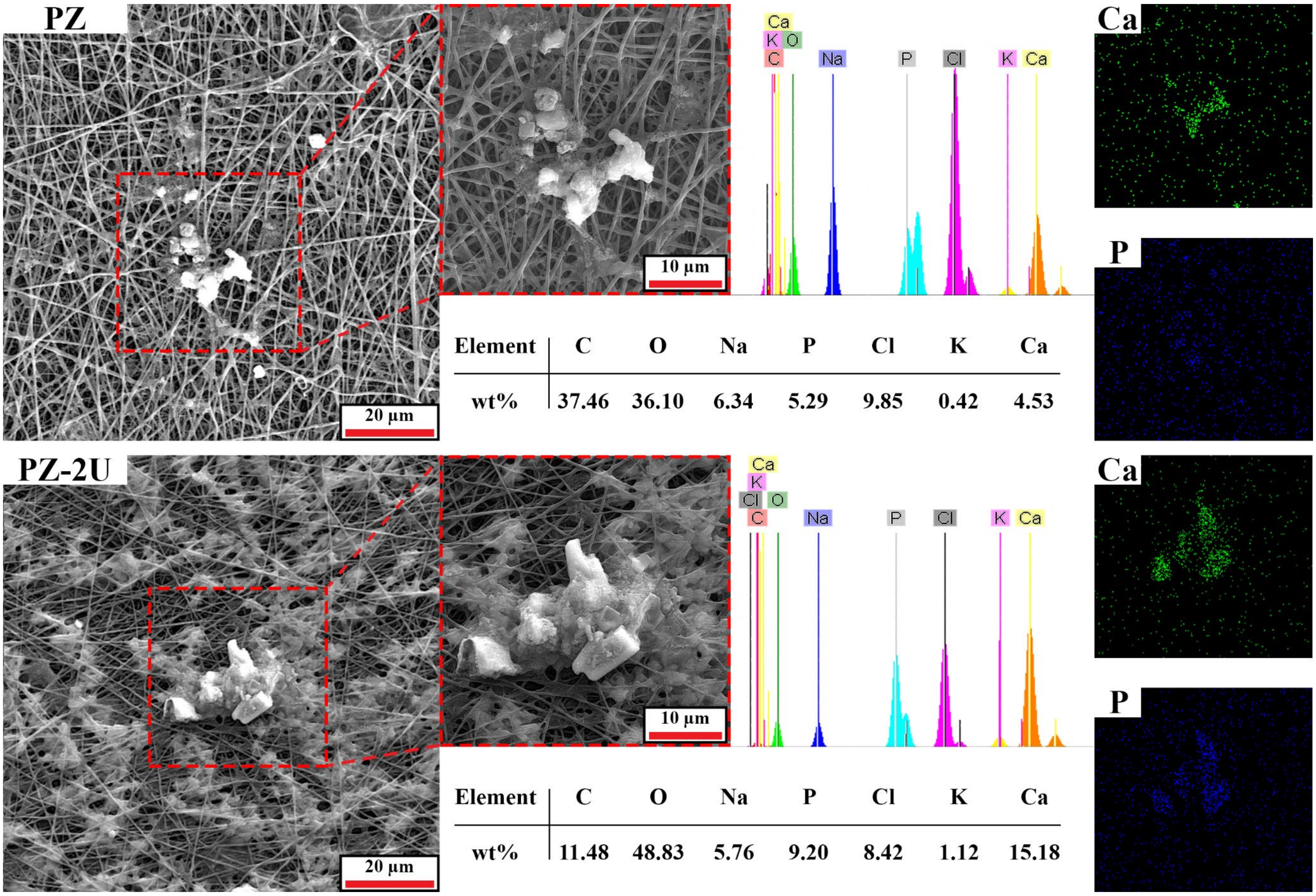

| Element | C | O | Na | P | Cl | K | Ca |
|---|---|---|---|---|---|---|---|
| wt% | 37.46 | 36.10 | 6.34 | 5.29 | 9.85 | 0.42 | 4.53 |

| Element | C | O | Na | P | Cl | K | Ca |
|---|---|---|---|---|---|---|---|
| wt% | 11.48 | 48.83 | 5.76 | 9.20 | 8.42 | 1.12 | 15.18 |

**Fig. 14** Biomineralization assessment on the surface of the PZ and PZ-2U electrospun scaffolds after 28 days of immersion in SBF solution: SEM images at different magnifications, EDS analysis of chemical elements, and EDS elemental maps of calcium (Ca) and phosphorous (P)

stable layer of depositions, which are more likely to crystallize and transform into hydroxyapatite [82].

### EDS

Figure 14 also displays EDS results, including quantitive amounts of chemical compounds and EDS mapping of sediments on the surface of the scaffolds after 28 days of immersion in the SBF. Regarding the EDS spectra, the presence of calcium (Ca) and phosphorous (P) in the depositions on both scaffolds was verified. The EDS findings revealed an increase in the elemental composition of Ca from 4.53 wt% to 15.18 wt% and P from 5.29 wt% to 9.20 wt% in the adsorbed deposits on the electrospun scaffolds as a result of UiO-66 addition. Since natural bone apatite sediments have a molar Ca/P ratio of approximately 1.67, a scaffold with a ratio closer to this is preferred [83]. Prior to hydroxyapatite's formation, the mineral discovered is most often amorphous calcium phosphate, which has Ca/P ratios less than 1.5. As matrix mineralization advances, the deposited mineral nodules are subjected to crystal maturation [84]. Calculating through the EDS Outputs, the molar Ca/P in the formed apatite-like sediments on the PZ and PZ-2U scaffolds equals 0.66 and 1.28, respectively. According to the Ca/P ratios found on the scaffolds, the mineral nodules formed are probably made of amorphous calcium phosphate, which may eventually fuse together to create hydroxyapatite as they mature [84]. Concerning the above results, the EDS analysis confirms that the bioactivity behavior of the PZ-2U electrospun scaffold is better than that of the PZ sample. Moris et al. [85] also showed a higher Ca/P ratio due to Zr-based MOF addition to gelatin scaffolds after submerging in an SBF solution for up to 28 days.

### XRD Analysis

The chemical structure of the sediments on the scaffolds' surface after 28 days of immersion in SBF has been evaluated using XRD analysis, and the results are demonstrated in Fig. 15. Based on the XRD spectra and comparison with the reference pattern of hydroxyapatite (PDF-Number: 96–901-3628) the formation of hydroxyapatite is verified by the presence of the peaks at 2θ = 10.86°, 16.97°, 23.14°, 25.68°, 28.54°, 31.74°, 45.56°, and 66.18° corresponded

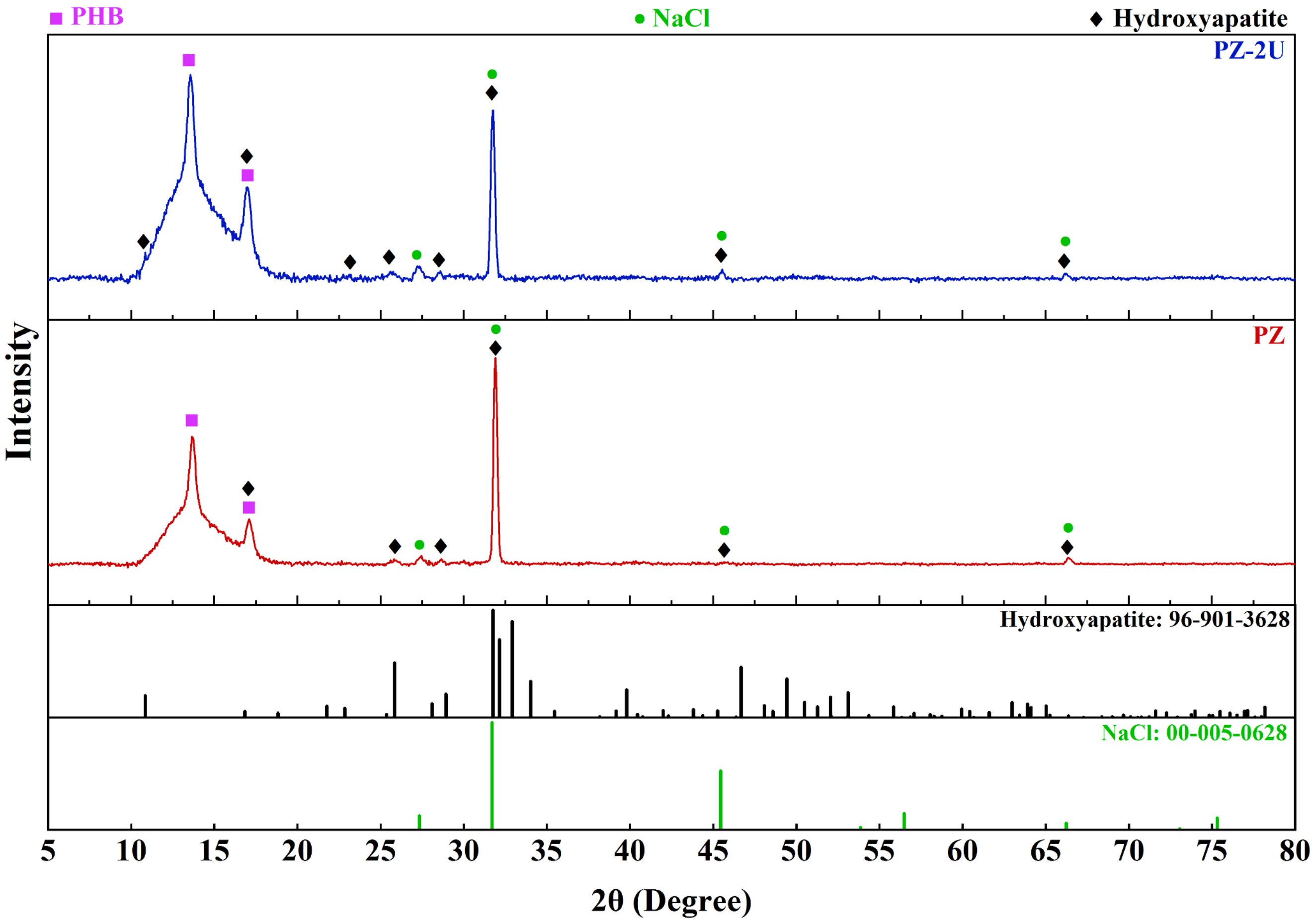

**Fig. 15** XRD patterns of the PZ and PZ-2U electrospun scaffolds after 28 days of immersion in SBF

to the (010), (011), (111), (002), (120), (121), (023), (242) crystallographic planes, respectively. Non-stoichiometric hydroxyapatite and low-crystalline apatite phases, which are most likely a combination of crystalline hydroxyapatite and amorphous calcium phosphates, may be the cause of the low-intense peaks [86]. In addition, regarding the reference pattern of calcium chloride (NaCl, PDF-Number: 96–901-3628), it is noted that calcium chloride was also formed on the surface of the scaffolds.

## Celluar Behavior Evaluations

### Cell Viability

The MTT assay results for the PZ and PZ-2U scaffolds are presented in Fig. 16. Based on the ISO10993-5:1999 standard, cell viability exceeding 75% may be regarded as posing no toxic risks to medical devices or cells [87]. According to the results, MG-63 cells exhibited over 85% viability and an increasing trend through all days on both scaffolds, indicating good biocompatibility, which may be attributed to the zein's ability to facilitate ECM absorption and create a suitable microenvironment for bone cells, which promotes cell migration, infiltration, and growth [7]. However, on the 3rd and 7th days of cultivation, the UiO-66 containing electrospun scaffold demonstrated significantly higher cell viability amounts in comparison with the PZ scaffold, suggesting that cell proliferation was being promoted in the presence of UiO-66 ($p < 0.05$). This enhanced cell viability can be a result of a more hydrophilic surface after UiO-66 addition. These findings align with previous research on Zr-based MOFs and materials that have shown desirable biocompatibility and low toxicity, leading to considerable growth in their biomedical applications [31, 85]. Investigations by Farboudi et al. [88] and Sadek et al. [4] revealed that UiO-66 particles had non-significant cytotoxic effects on MCF-7 and NIH-3T3 cells, respectively. Additionally, the study by Karakecili et al. [38] demonstrated that the chitosan scaffold containing UiO-66 MOF had greater optical density in the MTT assay compared to the pure chitosan scaffold. In another study, Chen et al. [89] confirmed the ability of Zr ions to enhance the in vitro proliferation of human osteoblasts.

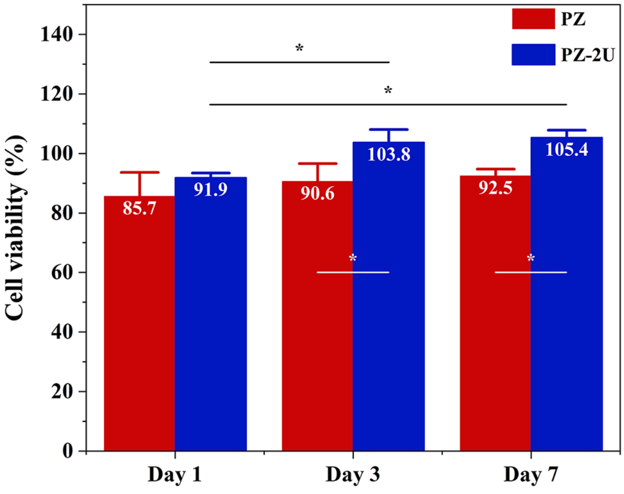

**Fig. 16** Viability of the MG-63 cells seeded on the PZ and PZ-2U electrospun scaffolds on the 1$^{st}$, 3$^{rd}$, and 7$^{th}$ days of the cultivation (*$p < 0.05$).

### Cell Attachment

The morphology of MG-63 cells on the PZ and PZ-2U scaffolds after 1 and 7 days of cultivation, carried out to evaluate the cell adhesion behavior, can be found in Fig. 17. By the 7th day, the cells were evenly spread out and well-attached to both scaffolds, displaying a typical fibroblastic morphology with indistinguishable boundaries between them. This excellent adherence may stem from promoted communication between the cells and the scaffolds resulting from zein presence, which is able to interact with cellular receptors and support cell growth [7]. The number of cells grew as the cultivation period progressed, which is aligned with the MTT results. Furthermore, discernible filopodia extensions and the formation of apatite-like deposits suggest ECM secretion [38]. It is worth noting that cell migration and penetration through the three-dimensional matrix with interconnected pores of the scaffolds can be confirmed by the appearance of the fibers on the cell surface.

As evident, the addition of UiO-66 resulted in increased cell density and more cells with spindle shape morphology observed on the PZ-2U scaffold on both the 1st and 7th days as compared to the PZ sample. The improved cell attachment in the PZ-2U scaffold can be related to the $Zr^{4+}$ ions, originating from missing linker defects in UiO-66, which have a positive effect due to the negatively charged nature of cells [72, 90]. So, the UiO-66 containing scaffolds have better cell attraction capabilities. Likewise, the inclusion of UiO-66 engendered thinner fibers with a higher surface-to-volume ratio, a rougher surface, and higher hydrophilicity, all of which contributed to better cell adhesion on the PZ-2U scaffold than the PZ one [7, 15, 59]. In previous research, Karakecili et al. [38] observed improved adhesion of the MC3T3-E1 cells after adding UiO-66 to the chitosan scaffold.

### DAPI Staining

Fluorescence images of the DAPI-stained MG-63 cells, which display the nucleus of the attached cells as blue dots on the PZ and PZ-2U scaffolds after 7 days of cell cultivation, are depicted in Fig. 18. As expected from the

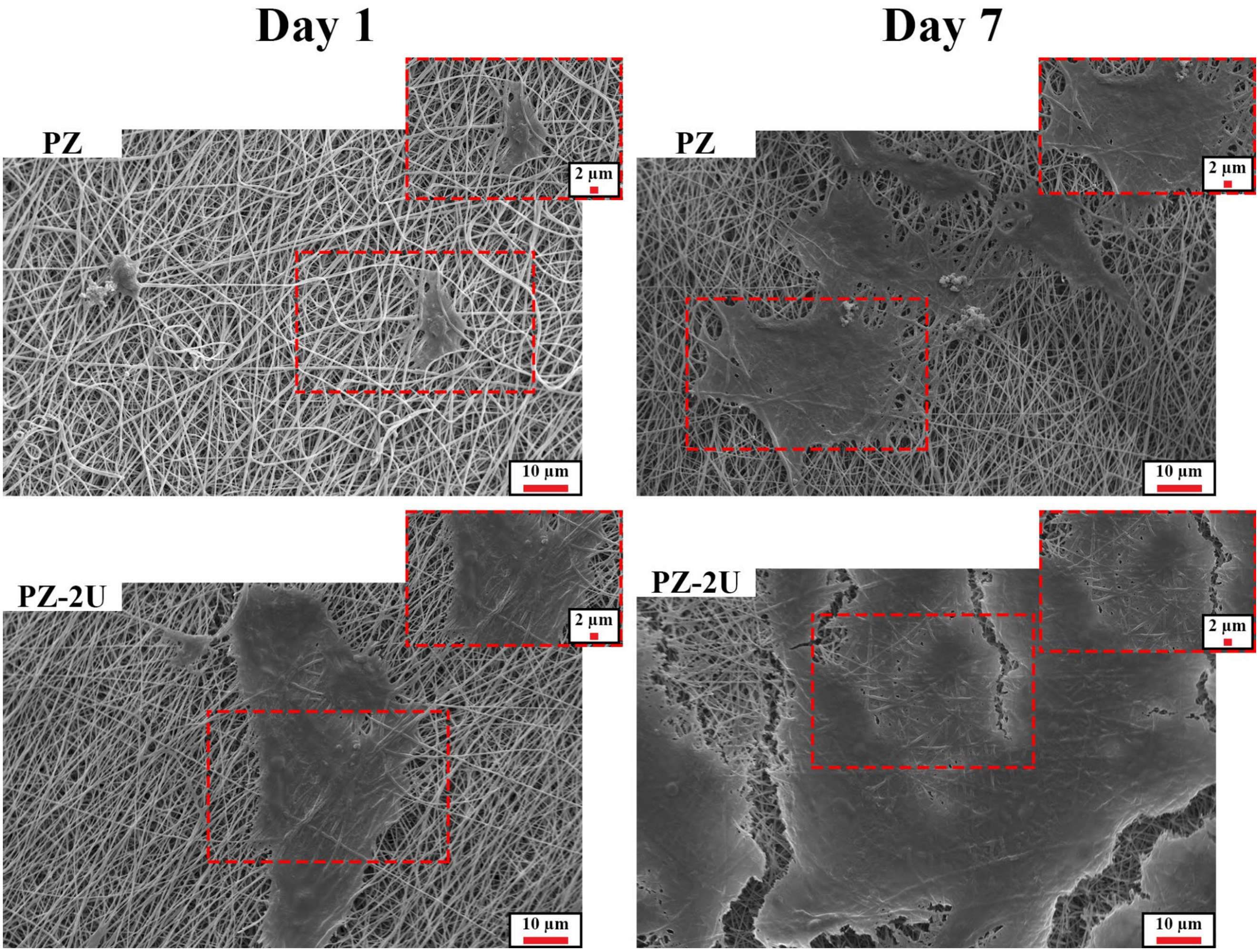

**Fig. 17** SEM images illustrating the MG-63 cell attachment seeded on the PZ and PZ-2U electrospun scaffolds on the 1st and 7th days of the cultivation

cell viability and attachment assessments, DAPI staining revealed a higher number of cells on the PZ-2U scaffold, proving improved proliferation of MG-63 cells compared to the PZ scaffold.

### ALP Activity

The activity of ALP, an exoenzyme that is attached to the osteoblasts' cell membrane and an early in vitro indicator of bone formation, was measured on days 7 and 14 after cell seeding to evaluate the impact of adding UiO-66 MOF on the osteogenic functionality of the MG-63 osteoblast [7, 85]. As can be seen in Fig. 19, MG-63 cells demonstrated significantly greater ALP activity on both scaffolds in comparison with the control group, with a noticeable upward trend between the two days ($p < 0.05$). Additionally, as supposed regarding the prior research [38], the UiO-66 incorporated scaffold showed statistically higher levels of ALP activity across all specified periods. The metallic inorganic Zr nodes, known to encourage the synthesis of biochemical osteoblastic markers, may account for this enhanced ALP activity [85].

### Alizarin Red Staining

The alizarin red staining of the MG-63 cells cultivated on the PZ and PZ-2U after 7 and 14 days of cell culture was performed to assess ECM mineralization, which is the final event of in vitro osteogenesis [7, 91]. As seen in Fig. 20 and in line with the previous carried out cellular assays, including MTT, cell attachment, DAPI staining, and ALP activity, the PZ-2U scaffold exhibited more and deeper deposition nodules, especially on day 14, which indicates intensified Ca mineralization of the MG-63 cells and highlights the positive influence of UiO-66 on cell maturation and in vitro bone formation [91]. In previous studies, Zr ions were shown to be able to enhance the quantity of mineralized matrix deposited [89].

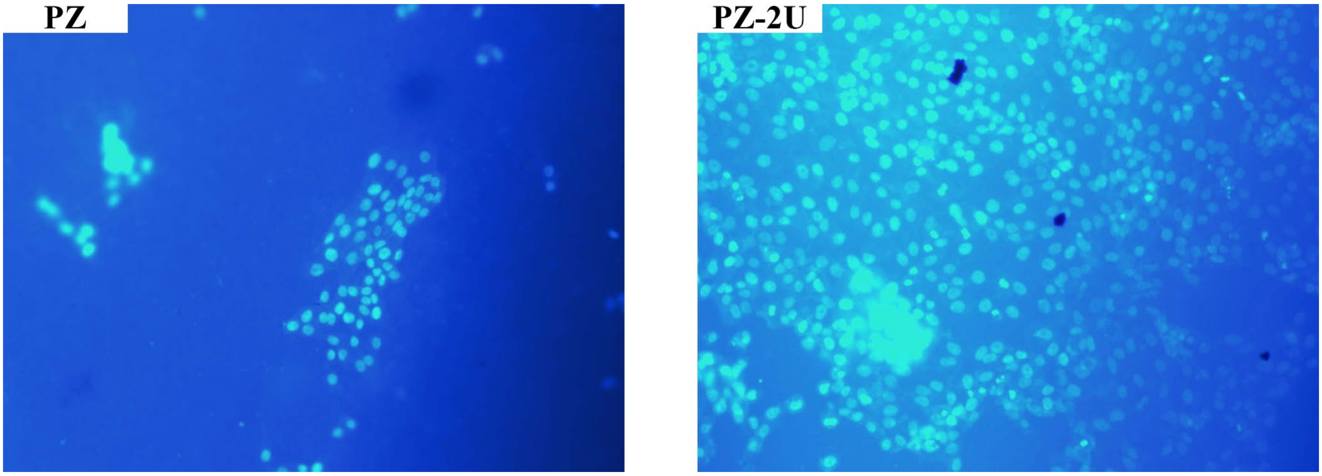

**Fig. 18** DAPI staining of the MG-63 cells seeded on the PZ and PZ-2U electrospun scaffolds on the 7th day of the cultivation.

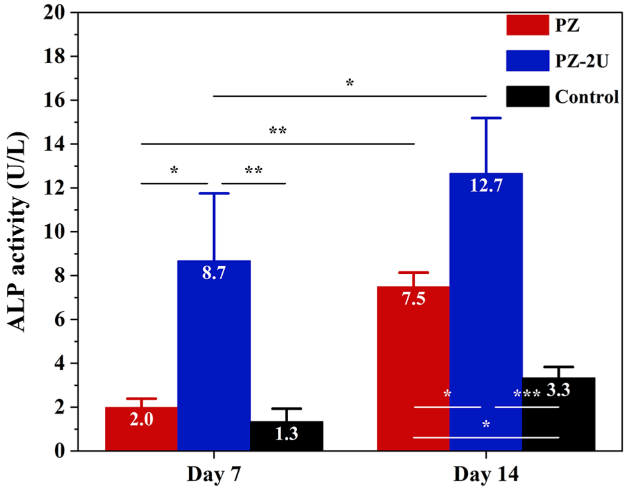

**Fig. 19** ALP activity of the MG-63 cells seeded on the PZ and PZ-2U scaffolds and control group on the 7th and 14th days of the cultivation (*$p < 0.05$, ** $p < 0.01$, *** $p < 0.001$).

### qRT-PCR Analysis

The expression of the collagenous and non-collagenous osteoblast-related markers, including COLI, RUNX2, and OCN, of the MG-63 cell after days 7, 14, and 21 of cultivation on the PZ and PZ-2U scaffolds was investigated using qRT-PCR assay to analyze the potential of the scaffolds to promote the osteogenic functions. The findings on the fold change expression of the COLI, RUNX2, and OCN genes are presented in Fig. 21. Regarding the results, the fold changes of all of the examined genes, even in the PZ scaffold, are greater than 1. This can be due to the presence of zein, which has been previously shown to have an influential ability to stimulate the expression of genes related to osteogenic differentiation in other studies [84, 92].

RUNX2 is considered an early marker of osteoblast differentiation and is an essential transcription factor in the differentiation of osteoblasts since it stimulates the production of COLI and OCN and has been proven to induce ALP activity [84, 93]. GLI1, PTCH1, and IHH expression in osteoblast progenitors and osteoblasts are directly regulated by RUNX2. As a result, Hedgehog signaling and RUNX2 control each other and promote osteoblast differentiation [94]. The expression of RUNX2 was significantly upregulated in the PZ-2U composite scaffold compared to the PZ alloy on day 14 ($p < 0.05$) [84, 93]. Zr ions of UiO-66 MOF can be responsible for this upregulation [4, 89]. It is worth mentioning that the enhanced ALP activity of the PZ-2U scaffold, which was discussed earlier, can now be explained by the increased RUNX2 expression. On day 21, the expression level of this gene experienced a decline in both groups of the scaffold. The same trend was also observed in the study of Karakecili et al. [38], where the UiO-66 addition to the chitosan scaffold enhanced the RUNX2 expression with a peak at day 14. According to the literature, RUNX2 expression is generally reduced in cultures aged 3 to 4 weeks, which serves as a critical marker of matrix maturation and mineralization [95].

COLI is known as an early marker corresponding to the proliferative phase and ECM deposition [84, 93]. As shown, with a peak on day 7, its expression was increased as a result of UiO-66 incorporation, especially on days 14 and 21, in which the differences are remarkable ($p < 0.05$). One possible source of COLI expression improvement in the UiO-66-containing group, which was also reported by other researchers, may be RUNX2's interaction with the promoter regions of genes specific to osteoblasts [4, 38]. The enhanced expression of COLI is consistent with MTT, cell attachment, and DAPI staining results.

OCN, as a non-collagenous protein, is associated with bone mineralization and matrix deposition and is expressed in the late stages [38, 93, 96]. The PZ-2U scaffold revealed

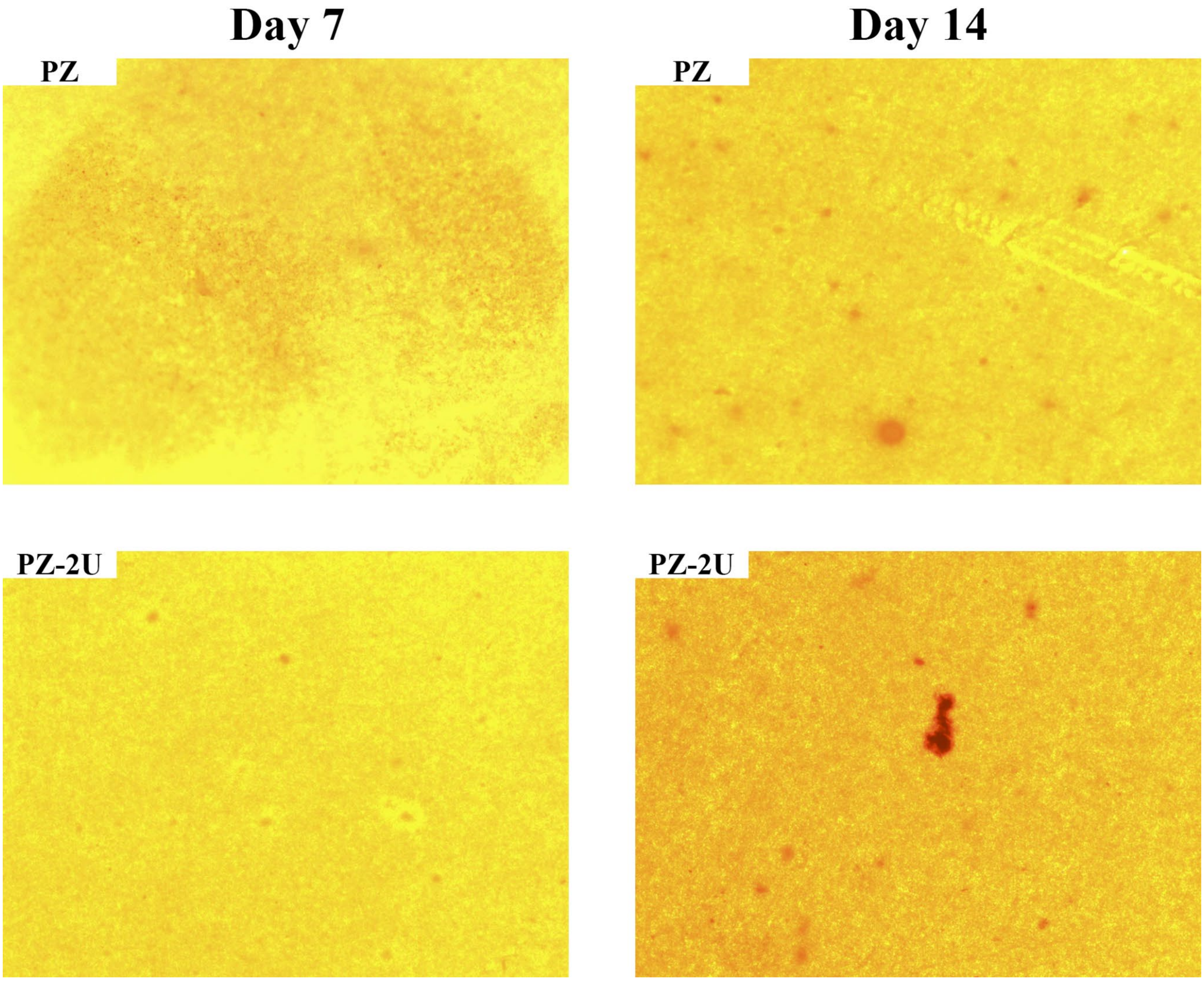

**Fig. 20** Alizarin red staining of the MG-63 cells seeded on the PZ and PZ-2U scaffolds on the 7th and 14th days of the cultivation

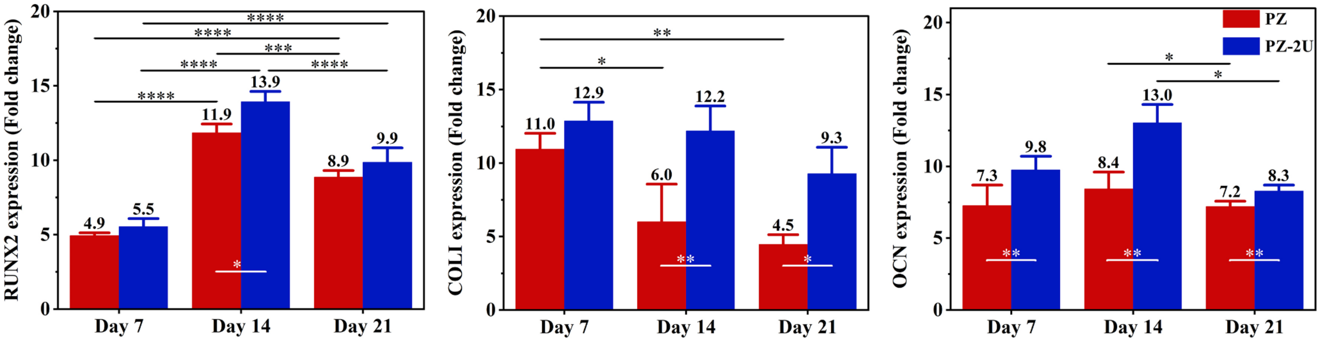

**Fig. 21** The RUNX2, COLI, and OCN gene expression of the MG-63 cells seeded on the PZ and PZ-2U scaffolds on the 7th, 14th, and 21st days of the cultivation (*$p < 0.05$, ** $p < 0.01$, *** $p < 0.001$, **** $p < 0.0001$).

significantly higher OCN expression on all days ($p < 0.05$), indicating a suitable environment for development and maturation towards the mineralization phase [84]. OCN expression peaked on day 14, while on day 21, its levels noticeably decreased. Previous research suggests that this decrease may be due to the completion of cell mineralization [4].

## Conclusion

Prior research has highlighted the outstanding characteristics of UiO-66 as a Zr-based MOF, such as exceptional chemical and physical stability, biocompatibility, and the ability to promote osteogenesis. In this investigation, a solvothermal method was employed to synthesize UiO-66 particles. The successful synthesis of UiO-66 was confirmed by FTIR, XRD, TEM, and FESEM analyses. Afterward, composite scaffolds comprising PHB-zein and UiO-66 in varying ratios (0, 0.5, 1, and 2 wt%) were fabricated via electrospinning. All the produced scaffolds possess 3D structures with appropriate porosity and interconnected pores. SEM, water contact measurement, and tensile strength evaluations were conducted to determine the optimum percentage of UiO-66 in the composite scaffolds. According to the results, the addition of 2 wt% UiO-66 led to a significant reduction in fiber diameter and water contact angle from 422 ± 90 nm to 368 ± 83 nm and from 139.4 ± 1.4° to 120.7 ± 3.5°, respectively. Although the ultimate tensile stress and Young's modulus were found to increase from 100.9 ± 0.8 MPa to 203.1 ± 0.2 and from 4.53 ± 0.41 MPa to 8.60 ± 0.99 MPa, respectively, the addition of the UiO-66 enhanced the brittleness of scaffolds, and elongation at break decreased from 100.9 ± 5.6% for the PZ scaffold to 66.0 ± 12.0% for the PZ-2U sample. Regarding these findings, the scaffold containing 2 wt% UiO-66 MOF was identified as the most effective among the composite ones. The physical presence and even distribution of the UiO-66 within the fabricated scaffolds were demonstrated through TEM analysis and EDS mapping. AFM revealed that the UiO-66 addition resulted in a rougher surface. The chemical presence of PHB, zein, and UiO-66 in the scaffolds, along with hydrogen and coordination bonds between UiO-66 crystals and PHB and zein, was shown in the FTIR inspection. TGA proved the quantity of the MOF in the scaffolds, and DCS exhibited a 2% increase in crystallinity degree, which was consistent with XRD results. MOF-containing scaffolds revealed an accelerated in vitro degradation rate and demonstrated enhanced biomineralization, indicating improved bioactivity behavior. The cellular examinations implied improved viability, proliferation, attachment, ALP activity, calcium deposition, ECM mineralization, and expression of osteoblast-related markers, including COLI, RUNX2, and OCN, of the MG-63 cells on the scaffolds containing UiO-66 compared to those without MOF. To conclude, along with strengthening the scaffold, the inclusion of UiO-66 also had a stimulatory impact on osteogenesis. Consequently, the PHB-zein/UiO-66 composite scaffold holds great promise for applications in bone tissue engineering.

**Acknowledgements** We would like to thank Isfahan University of Medical Sciences and the Department of Biomaterials and Tissue Engineering for providing the equipment for this experiment. This project has received funding from Isfahan University of Medical Sciences, Isfahan, Iran, under grant number 1400434.

**Author Contributions** Saeid Ghasemi: Conceptualization, Methodology, Validation, Formal analysis, Investigation, Writing - Original Draft, Visualization. Mahdie Esmaeili: Investigation, Validation. Mohammad Dinari: Methodology, Validation, Writing - Review & Editing, Resources. Arezou Dabiri: Investigation. Saeed Karbasi: Conceptualization, Validation, Writing - Review & Editing, Supervision, Resources, Funding acquisition.

**Data Availability** No datasets were generated or analysed during the current study.

## Declarations

**Competing Interests** The authors declare no competing interests.

## References

1. Xue N, Ding X, Huang R, Jiang R, Huang H, Pan X et al (2022) Bone tissue engineering in the treatment of bone defects. Pharmaceuticals (Basel) 15(7). https://doi.org/10.3390/ph15070879
2. Tavakoli MR, Karbasi S, Soleymani Eil Bakhtiari S (2020 ) Evaluation of physical, mechanical, and biodegradation of chitosan/graphene oxide composite as bone substitutes. Polymer-Plastics Technol Mat 59(4):430–440. https://doi.org/10.1080/25740881.2019.1653467
3. Farnaghi M, Poursamar SA, Farzan M, Farzan M, Kouhi M, Rafienia M (2025) Enhancing the biological characteristics of aminolysis surface modified 3D printed nanocomposite polycaprolactone/nanohydroxyapatite scaffold via gelatin biomacromolecule immobilization: an in vitro and in vivo study. Colloids Surf B Biointerfaces 249:11450. https://doi.org/10.1016/j.colsurfb.2025.114505
4. Sadek AA, Abd-Elkareem M, Abdelhamid HN, Moustafa S, Hussein K (2022) Enhancement of critical-sized bone defect regeneration using UiO-66 nanomaterial in rabbit femurs. BMC Vet Res 18(1):260. https://doi.org/10.1186/s12917-022-03347-9
5. Koons GL, Diba M, Mikos AG (2020) Materials design for bone-tissue engineering. Nat Reviews Mater 5(8):584–603. https://doi.org/10.1038/s41578-020-0204-2
6. Bahremandi-Toloue E, Mohammadalizadeh Z, Mukherjee S, Karbasi S (2022) Incorporation of inorganic bioceramics into electrospun scaffolds for tissue engineering applications: a review. Ceram Int 48(7):8803–8837. https://doi.org/10.1016/j.ceramint.2021.12.125
7. Ghasemi S, Alibabaie A, Saberi R, Esmaeili M, Semnani D, Karbasi S (2023) Evaluation of the effects of zein incorporation on physical, mechanical, and biological properties of polyhydroxybutyrate electrospun scaffold for bone tissue engineering applications. Int J Biol Macromol 253(Pt 3):126843. https://doi.org/10.1016/j.ijbiomac.2023.126843
8. Rahman M, Dip TM, Haase T, Truong YB, Le TC, Houshyar S (2023) Fabrication of zein-based fibrous scaffolds for biomedical applications—a review. Macromol Mater Eng 308(12). https://doi.org/10.1002/mame.202300175
9. Soleymani Eil Bakhtiari S, Karbasi S, Toloue EB (2021) Modified poly(3-hydroxybutyrate)-based scaffolds in tissue engineering applications: a review. Int J Biol Macromol 166:986–998. https://doi.org/10.1016/j.ijbiomac.2020.10.255

10. Chernozem RV, Guselnikova O, Surmeneva MA, Postnikov PS, Abalymov AA, Parakhonskiy BV et al (2020) Diazonium chemistry surface treatment of piezoelectric polyhydroxybutyrate scaffolds for enhanced osteoblastic cell growth. Appl Mater Today 20. https://doi.org/10.1016/j.apmt.2020.100758
11. Esmaeili M, Ghasemi S, Shariati L, Karbasi S (2024) Evaluating the osteogenic properties of polyhydroxybutyrate-zein/multiwalled carbon nanotubes (MWCNTs) electrospun composite scaffold for bone tissue engineering applications. Int J Biol Macromol 276(Pt 2):133829. https://doi.org/10.1016/j.ijbiomac.2024.133829
12. Tehrani AH, Zadhoush A, Karbasi S, Khorasani SN (2010) Experimental investigation of the governing parameters in the electrospinning of poly(3-hydroxybutyrate) scaffolds: structural characteristics of the pores. J Appl Polym Sci 118(5):2682–2689. https://doi.org/10.1002/app.32620
13. Sadeghi D, Karbasi S, Razavi S, Mohammadi S, Shokrgozar MA, Bonakdar S (2016) Electrospun poly(hydroxybutyrate)/chitosan blend fibrous scaffolds for cartilage tissue engineering. J Appl Polym Sci 133(47). https://doi.org/10.1002/app.44171
14. Soleymani E, Bakhtiari S, Karbasi S (2024) Keratin-containing scaffolds for tissue engineering applications: a review. J Biomater Sci Polym Ed 35(6):916–965. https://doi.org/10.1080/09205063.2024.2311450
15. Mohammadalipour M, Behzad T, Karbasi S, Mohammadalipour Z (2022) Optimization and characterization of polyhydroxybutyrate/lignin electro-spun scaffolds for tissue engineering applications. Int J Biol Macromol 218:317–334. https://doi.org/10.1016/j.ijbiomac.2022.07.139
16. Ramanathan G, Singaravelu S, Raja MD, Nagiah N, Padmapriya P, Ruban K et al (2016) Fabrication and characterization of a collagen coated electrospun poly(3-hydroxybutyric acid)–gelatin nanofibrous scaffold as a soft bio-mimetic material for skin tissue engineering applications. RSC Adv 6(10):7914–7922. https://doi.org/10.1039/c5ra19529b
17. Asl MA, Karbasi S, Beigi-Boroujeni S, Benisi Z, S., Saeed M (2021) Evaluation of the effects of starch on polyhydroxybutyrate electrospun scaffolds for bone tissue engineering applications. Int J Biol Macromol 191:500–513. https://doi.org/10.1016/j.ijbiomac.2021.09.078
18. Ghadirian S, Karbasi S, Kharazi AZ, Setayeshmehr M (2023) Evaluation of the effects of halloysite nanotubes on physical, mechanical, and biological properties of polyhydroxy butyrate electrospun scaffold for cartilage tissue engineering applications. J Polym Environ 32(3):1170–1187. https://doi.org/10.1007/s10924-023-03024-4
19. Motiee ES, Karbasi S, Bidram E, Sheikholeslam M (2023) Investigation of physical, mechanical and biological properties of polyhydroxybutyrate-chitosan/graphene oxide nanocomposite scaffolds for bone tissue engineering applications. Int J Biol Macromol 247:125593. https://doi.org/10.1016/j.ijbiomac.2023.125593
20. Amnieh YA, Ghadirian S, Mohammadi N, Shadkhast M, Karbasi S (2023) Evaluation of the effects of chitosan nanoparticles on polyhydroxy butyrate electrospun scaffolds for cartilage tissue engineering applications. Int J Biol Macromol 249:126064. https://doi.org/10.1016/j.ijbiomac.2023.126064
21. Mohammadi N, Amnieh A, Ghasemi Y, Karbasi S, S., Vaezifar S (2024) Evaluation of the effects of decellularized extracellular matrix nanoparticles incorporation on the polyhydroxybutyrate/nano chitosan electrospun scaffold for cartilage tissue engineering. Int J Biol Macromol 273(Pt 2):133217. https://doi.org/10.1016/j.ijbiomac.2024.133217
22. Khoroushi M, Foroughi MR, Karbasi S, Hashemibeni B, Khademi AA (2018) Effect of polyhydroxybutyrate/chitosan/bioglass nanofiber scaffold on proliferation and differentiation of stem cells from human exfoliated deciduous teeth into odontoblast-like cells. Mater Sci Eng C Mater Biol Appl 89:128–139. https://doi.org/10.1016/j.msec.2018.03.028
23. Toloue EB, Mohammadalipour M, Mukherjee S, Karbasi S (2024) Ultra-thin electrospun nanocomposite scaffold of poly (3-hydroxybutyrate)-chitosan/magnetic mesoporous bioactive glasses for bone tissue engineering applications. Int J Biol Macromol 254(Pt 2):127860. https://doi.org/10.1016/j.ijbiomac.2023.127860
24. Montazeri M, Karbasi S, Foroughi MR, Monshi A, Ebrahimi-Kahrizsangi R (2015) Evaluation of mechanical property and bioactivity of nano-bioglass 45S5 scaffold coated with poly-3-hydroxybutyrate. J Mater Sci Mater Med 26(2):62. https://doi.org/10.1007/s10856-014-5369-z
25. Foroughi MR, Karbasi S, Ebrahimi-Kahrizsangi R (2011) Physical and mechanical properties of a poly-3-hydroxybutyrate-coated nanocrystalline hydroxyapatite scaffold for bone tissue engineering. J Porous Mater 19(5):667–675. https://doi.org/10.1007/s10934-011-9518-1
26. Popov Pda, Cunha MD, Caracciolo PC, Abraham GA (2021) Latest advances in electrospun plant-derived protein scaffolds for biomedical applications. Curr Opin Biomedical Eng 18. https://doi.org/10.1016/j.cobme.2020.07.003
27. Tortorella S, Maturi M, Buratti V, Vozzolo V, Locatelli G, Sambri E, L., et al (2021) Zein as a versatile biopolymer: different shapes for different biomedical applications. RSC Adv 11(62):39004–39026. https://doi.org/10.1039/d1ra07424e
28. Pérez-Guzmán CJ, Castro-Muñoz R (2020) A review of zein as a potential biopolymer for tissue engineering and nanotechnological applications. Processes 8(11). https://doi.org/10.3390/pr8111376
29. Abánades Lázaro I, Forgan RS (2019) Application of zirconium MOFs in drug delivery and biomedicine. Coord Chem Rev 380:230–259. https://doi.org/10.1016/j.ccr.2018.09.009
30. Wong HL, Tsang CY, Beyer S (2023) Metal-organic frameworks (MOFs) and their composites as emerging biomaterials for osteoarthritis treatment. Biomimetics (Basel) 8(1). https://doi.org/10.3390/biomimetics8010097
31. Pourmadadi M, Eshaghi MM, Ostovar S, Shamsabadipour A, Safakhah S, Mousavi MS et al (2022) UiO-66 metal-organic framework nanoparticles as gifted MOFs to the biomedical application: a comprehensive review. J Drug Deliv Sci Technol 76. https://doi.org/10.1016/j.jddst.2022.103758
32. Asadniaye Fardjahromi M, Nazari H, Ahmadi Tafti SM, Razmjou A, Mukhopadhyay S, Warkiani ME (2022) Metal-organic framework-based nanomaterials for bone tissue engineering and wound healing. Mater Today Chem 23. https://doi.org/10.1016/j.mtchem.2021.100670
33. Li X, Shu X, Shi Y, Li H, Pei X (2023) MOFs and bone: application of MOFs in bone tissue engineering and bone diseases. Chin Chem Lett 34(7). https://doi.org/10.1016/j.cclet.2022.107986
34. Wang X, Zhou X, Yang K, Li Q, Wan R, Hu G et al (2021) Peroxidase- and UV-triggered oxidase mimetic activities of the UiO-66-NH(2)/chitosan composite membrane for antibacterial properties. Biomater Sci 9(7):2647–2657. https://doi.org/10.1039/d0bm01960g
35. Cavka JH, Jakobsen S, Olsbye U, Guillou N, Lamberti C, Bordiga S et al (2008) A new zirconium inorganic building brick forming metal organic frameworks with exceptional stability. J Am Chem Soc 130(42):13850–13851. https://doi.org/10.1021/ja8057953
36. Winarta J, Shan B, McIntyre SM, Ye L, Wang C, Liu J et al (2019) A decade of UiO-66 research: a historic review of dynamic structure, synthesis mechanisms, and characterization techniques of an archetypal metal–organic framework. Cryst Growth Des 20(2):1347–1362. https://doi.org/10.1021/acs.cgd.9b00955

37. Gu Q, Ng HY, Zhao D, Wang J (2020) Metal–Organic frameworks (MOFs)-boosted filtration membrane technology for water sustainability. APL Mater 8(4). https://doi.org/10.1063/5.0002905
38. Karakecili A, Topuz B, Ersoy FS, Sahin T, Gunyakti A, Demirtas TT (2022) UiO-66 metal-organic framework as a double actor in chitosan scaffolds: antibiotic carrier and osteogenesis promoter. Biomater Adv 136:212757. https://doi.org/10.1016/j.bioadv.2022.212757
39. Jarai BM, Stillman Z, Attia L, Decker GE, Bloch ED, Fromen CA (2020) Evaluating UiO-66 metal-organic framework nanoparticles as acid-sensitive carriers for pulmonary drug delivery applications. ACS Appl Mater Interfaces 12(35):38989–39004. https://doi.org/10.1021/acsami.0c10900
40. Wang W, Wang L, Li Z, Xie Z (2016) BODIPY-containing nanoscale metal-organic frameworks for photodynamic therapy. Chem Commun (Camb) 52(31):5402–5405. https://doi.org/10.1039/c6cc01048b
41. Ghasemi-Mobarakeh L, Semnani D, Morshed M (2007) A novel method for porosity measurement of various surface layers of nanofibers mat using image analysis for tissue engineering applications. J Appl Polym Sci 106(4):2536–2542. https://doi.org/10.1002/app.26949
42. Kokubo T, Takadama H (2006) How useful is SBF in predicting in vivo bone bioactivity? Biomaterials 27(15):2907–2915. https://doi.org/10.1016/j.biomaterials.2006.01.017
43. Chen C, Chen D, Xie S, Quan H, Luo X, Guo L (2017) Adsorption behaviors of organic micropollutants on zirconium metal-organic framework UiO-66: analysis of surface interactions. ACS Appl Mater Interfaces 9(46):41043–41054. https://doi.org/10.1021/acsami.7b13443
44. Azhar MR, Abid HR, Periasamy V, Sun H, Tade MO, Wang S (2017) Adsorptive removal of antibiotic sulfonamide by UiO-66 and ZIF-67 for wastewater treatment. J Colloid Interface Sci 500:88–95. https://doi.org/10.1016/j.jcis.2017.04.001
45. Majid MF, Zaid M, Abd Shukur HF, Ahmad MF, A., Jumbri K (2023) Host-guest interactions of zirconium-based metal-organic framework with ionic liquid. Molecules 28(6). https://doi.org/10.3390/molecules28062833
46. ElHussein EAA, Şahin S, Bayazit ŞS (2020) Removal of carbamazepine using UiO-66 and UiO-66/graphene nanoplatelet composite. J Environ Chem Eng 8(4):103898. https://doi.org/10.1016/j.jece.2020.103898
47. Aden SF, Mahmoud LAM, Ivanovska EH, Terry LR, Ting VP, Katsikogianni MG et al (2023) Controlled delivery of ciprofloxacin using zirconium-based MOFs and poly-caprolactone composites. J Drug Deliv Sci Technol 88. https://doi.org/10.1016/j.jddst.2023.104894
48. Kim H-G, Choi K, Lee K, Lee S, Jung K-W, Choi J-W (2021) Controlling the structural robustness of zirconium-based metal organic frameworks for efficient adsorption on tetracycline antibiotics. Water 13(13). https://doi.org/10.3390/w13131869
49. Valenzano L, Civalleri B, Chavan S, Bordiga S, Nilsen MH, Jakobsen S et al (2011) Disclosing the complex structure of UiO-66 metal organic framework: a synergic combination of experiment and theory. Chem Mater 23(7):1700–1718
50. Han Y, Liu M, Li K, Zuo Y, Wei Y, Xu S et al (2015) Facile synthesis of morphology and size-controlled zirconium metal–organic framework UiO-66: the role of hydrofluoric acid in crystallization. CrystEngComm 17(33):6434–6440. https://doi.org/10.1039/c5ce00729a
51. Lee S, Burgi HB, Alshmimri SA, Yaghi OM (2018) Impact of disordered guest-framework interactions on the crystallography of metal-organic frameworks. J Am Chem Soc 140(28):8958–8964. https://doi.org/10.1021/jacs.8b05271
52. Wu R, Qian X, Zhou K, Liu H, Yadian B, Wei J et al (2013) Highly dispersed au nanoparticles immobilized on Zr-based metal–organic frameworks as heterostructured catalyst for CO oxidation. J Mater Chem A 1(45):14294–14299. https://doi.org/10.1039/c3ta13114a
53. Jajko G, Gutiérrez-Sevillano JJ, Sławek A, Szufla M, Kozyra P, Matoga D et al (2022) Water adsorption in ideal and defective UiO-66 structures. Microporous Mesoporous Mater 330. https://doi.org/10.1016/j.micromeso.2021.111555
54. Jajko G, Calero S, Kozyra P, Makowski W, Slawek A, Gil B et al (2022) Defect-induced tuning of polarity-dependent adsorption in hydrophobic-hydrophilic UiO-66. Commun Chem 5(1):120. https://doi.org/10.1038/s42004-022-00742-z
55. Li X, Zhang H, Wang P, Hou J, Lu J, Easton CD et al (2019) Fast and selective fluoride ion conduction in sub-1-nanometer metal-organic framework channels. Nat Commun 10(1):2490. https://doi.org/10.1038/s41467-019-10420-9
56. Fu Q, Zhang W, Muhammad IP, Chen X, Zeng Y, Wang B et al (2021) Coaxially Electrospun PAN/HCNFs@PVDF/UiO-66 composite separator with high strength and thermal stability for lithium-ion battery. Microporous Mesoporous Mater 311. https://doi.org/10.1016/j.micromeso.2020.110724
57. Ahmadijokani F, Molavi H, Bahi A, Wuttke S, Kamkar M, Rojas OJ et al (2023) Electrospun nanofibers of chitosan/polyvinyl alcohol/UiO-66/nanodiamond: versatile adsorbents for wastewater remediation and organic dye removal. Chem Eng J 457. https://doi.org/10.1016/j.cej.2022.141176
58. Heidarkhan Tehrani A, Zadhoush A, Karbasi S, Sadeghi-Aliabadi H (2010) Scaffold percolative efficiency: in vitro evaluation of the structural criterion for electrospun mats. J Mater Sci Mater Med 21(11):2989–2998. https://doi.org/10.1007/s10856-010-4149-7
59. Deligianni DD, Katsala ND, Koutsoukos PG, Missirlis YF (2001) Effect of surface roughness of hydroxyapatite on human bone marrow cell adhesion, proliferation, differentiation and detachment strength. Biomaterials 22(1):87–96. https://doi.org/10.1016/s0142-9612(00)00174-5
60. Hatano K, Inoue H, Kojo T, Matsunaga T, Tsujisawa T, Uchiyama C et al (1999) Effect of surface roughness on proliferation and alkaline phosphatase expression of rat calvarial cells cultured on polystyrene. Bone 25(4):439–445. https://doi.org/10.1016/s8756-3282(99)00192-1
61. Xu J, Guo B-H, Yang R, Wu Q, Chen G-Q, Zhang Z-M (2002) In situ FTIR study on melting and crystallization of polyhydroxyalkanoates. Polymer 43(25):6893–6899. https://doi.org/10.1016/s0032-3861(02)00615-8
62. Ghadirian S, Karbasi S (2023) Evaluation of the effects of halloysite nanotube on polyhydroxybutyrate - chitosan electrospun scaffolds for cartilage tissue engineering applications. Int J Biol Macromol 233:123651. https://doi.org/10.1016/j.ijbiomac.2023.123651
63. Chernozem RV, Pariy IO, Pryadko A, Bonartsev AP, Voinova VV, Zhuikov VA et al (2022) A comprehensive study of the structure and piezoelectric response of biodegradable polyhydroxybutyrate-based films for tissue engineering applications. Polym J 54(10):1225–1236. https://doi.org/10.1038/s41428-022-00662-8
64. Yin Y, Wang Y, Meng L (2021) UIO-66 as nucleating agent on the crystallization behavior and properties of poly(ethylene terephthalate). Polym (Basel) 13(14). https://doi.org/10.3390/polym13142266
65. Jrad A, Al Sabeh G, Hannouche K, Al Natour R, Haidar O, Sammoury H et al (2023) Critical role of defects in UiO-66 nanocrystals for catalysis and water remediation. ACS Appl Nano Mater 6(20):18698–18720. https://doi.org/10.1021/acsanm.3c03787
66. Yang Y, Zan J, Yang W, Qi F, He C, Huang S et al (2020) Metal organic frameworks as a compatible reinforcement in a

biopolymer bone scaffold. Mater Chem Front 4(3):973–984. https://doi.org/10.1039/c9qm00772e

67. Wu H, Yildirim T, Zhou W (2013) Exceptional mechanical stability of highly porous zirconium metal-organic framework UiO-66 and its important implications. J Phys Chem Lett 4(6):925–930. https://doi.org/10.1021/jz4002345
68. de Lima HHC, da Silva CTP, Kupfer VL, de C. Rinaldi J, Kioshima ES, Mandelli D et al (2021) Synthesis of resilient hybrid hydrogels using UiO-66 MOFs and alginate (hydroMOFs) and their effect on mechanical and matter transport properties. Carbohydr Polym 251:116977. https://doi.org/10.1016/j.carbpol.2020.116977
69. Salehi S, Tavakoli M, Mirhaj M, Varshosaz J, Labbaf S, Karbasi S et al (2023) A 3D printed polylactic acid-Baghdadite nanocomposite scaffold coated with microporous chitosan-VEGF for bone regeneration applications. Carbohydr Polym 312:120787. https://doi.org/10.1016/j.carbpol.2023.120787
70. Shen R, Yan TH, Ma R, Joseph E, Quan Y, Zhou HC et al (2021) Flammability and thermal kinetic analysis of UiO-66-based PMMA Polymer composites. Polym (Basel) 13(23). https://doi.org/10.3390/polym13234113
71. Molefe LY, Musyoka NM, Ren J, Langmi HW, Mathe M, Ndungu PG (2020) Effect of inclusion of MOF-polymer composite onto a carbon foam material for hydrogen storage application. J Inorg Organomet Polym Mater 31(1):80–88. https://doi.org/10.1007/s10904-020-01701-8
72. Wu H, Chua YS, Krungleviciute V, Tyagi M, Chen P, Yildirim T et al (2013) Unusual and highly tunable missing-linker defects in zirconium metal-organic framework UiO-66 and their important effects on gas adsorption. J Am Chem Soc 135(28):10525–10532. https://doi.org/10.1021/ja404514r
73. Katz MJ, Brown ZJ, Colon YJ, Siu PW, Scheidt KA, Snurr RQ et al (2013) A facile synthesis of UiO-66, UiO-67 and their derivatives. Chem Commun (Camb) 49(82):9449–9451. https://doi.org/10.1039/c3cc46105j
74. Ahmed M, Al-Hadeethi YM, Alshahrie A, Kutbee AT, Al-Hossainy AF, Shaaban ER (2022) Thermal analysis and non-isothermal crystallization kinetic of PET/UiO-66 nanocomposite. J Mater Res Technol 18:3492–3501. https://doi.org/10.1016/j.jmrt.2022.03.063
75. Bose S, Roy M, Bandyopadhyay A (2012) Recent advances in bone tissue engineering scaffolds. Trends Biotechnol 30(10):546–554. https://doi.org/10.1016/j.tibtech.2012.07.005
76. Shuai C, Wang Z, Zhang H, Jia J, Huang L, Wang D et al (2022) Biosoluble ceramic fiber reinforced poly(L-lactic acid) bone scaffold: degradation and bioactivity. Npj Mater Degrad 6(1). https://doi.org/10.1038/s41529-022-00297-3
77. Trushina DB, Sapach AY, Burachevskaia OA, Medvedev PV, Khmelenin DN, Borodina TN et al (2022) Doxorubicin-loaded core-shell UiO-66@SiO(2) metal-organic frameworks for targeted cellular uptake and cancer treatment. Pharmaceutics 14(7). https://doi.org/10.3390/pharmaceutics14071325
78. Movahedi M, Karbasi S (2022) Electrospun halloysite nanotube loaded polyhydroxybutyrate-starch fibers for cartilage tissue engineering. Int J Biol Macromol 214:301–311. https://doi.org/10.1016/j.ijbiomac.2022.06.072
79. Ghafari F, Karbasi S, Baghaban Eslaminejad M, Sayahpour FA, Kalantari N (2023) Biological evaluation and osteogenic potential of polyhydroxybutyrate-keratin/Al(2)O(3) electrospun nanocomposite scaffold: a novel bone regeneration construct. Int J Biol Macromol 242(Pt 1):124602. https://doi.org/10.1016/j.ijbiomac.2023.124602
80. Asl MA, Karbasi S, Beigi-Boroujeni S, Benisi SZ, Saeed M (2022) Polyhydroxybutyrate-starch/carbon nanotube electrospun nanocomposite: a highly potential scaffold for bone tissue engineering applications. Int J Biol Macromol 223(Pt A):524–542. https://doi.org/10.1016/j.ijbiomac.2022.11.023
81. Mohammadalipour M, Karbasi S, Behzad T, Mohammadalipour Z, Zamani M (2022) Effect of cellulose nanofibers on polyhydroxybutyrate electrospun scaffold for bone tissue engineering applications. Int J Biol Macromol 220:1402–1414. https://doi.org/10.1016/j.ijbiomac.2022.09.118
82. Mirmusavi MH, Ahmadian M, Karbasi S (2022) Polycaprolactone-chitosan/multi-walled carbon nanotube: a highly strengthened electrospun nanocomposite scaffold for cartilage tissue engineering. Int J Biol Macromol 209(Pt B):1801–1814. https://doi.org/10.1016/j.ijbiomac.2022.04.152
83. Wu X, Walsh K, Hoff BL, Camci-Unal G (2020) Mineralization of biomaterials for bone tissue engineering. Bioeng (Basel) 7(4). https://doi.org/10.3390/bioengineering7040132
84. Cardenas Turner J, Collins G, Blaber EA, Almeida EAC, Arinzeh TL (2020) Evaluating the cytocompatibility and differentiation of bone progenitors on electrospun zein scaffolds. J Tissue Eng Regen Med 14(1):173–185. https://doi.org/10.1002/term.2984
85. Moris H, Ghaee A, Sharifloo MM, Hosseini I, Nouri-Felekori M (2024) Gelatin- zirconium based metal-organic framework (MOF 801) nanocomposite scaffold for bone tissue engineering. Ceram Int 50(13):23986–23998. https://doi.org/10.1016/j.ceramint.2024.04.129
86. Wan C, Frydrych M, Chen B (2011) Strong and bioactive gelatin–graphene oxide nanocomposites. Soft Matter 7(13). https://doi.org/10.1039/c1sm05321c
87. Soleymani Eil Bakhtiari S, Bakhsheshi-Rad HR, Karbasi S, Razzaghi M, Tavakoli MR, Ismail AF,Sharif S, RamaKrishna S, Chen X, Berto F (2021) 3-DimensionalPrinting of Hydrogel-Based Nanocomposites: A Comprehensive Review on the Technology Description, Properties, and Applications. Adv Eng Mat 23(10):2100477. https://doi.org/10.1002/adem.202100477
88. Farboudi A, Mahboobnia K, Chogan F, Karimi M, Askari A, Banihashem S et al (2020) UiO-66 metal organic framework nanoparticles loaded carboxymethyl chitosan/poly ethylene oxide/polyurethane core-shell nanofibers for controlled release of doxorubicin and folic acid. Int J Biol Macromol 150:178–188. https://doi.org/10.1016/j.ijbiomac.2020.02.067
89. Chen Y, Roohani-Esfahani SI, Lu Z, Zreiqat H, Dunstan CR (2015) Zirconium ions up-regulate the BMP/SMAD signaling pathway and promote the proliferation and differentiation of human osteoblasts. PLoS ONE 10(1):e0113426. https://doi.org/10.1371/journal.pone.0113426
90. Ferrari M, Cirisano F, Morán MC (2019) Mammalian cell behavior on hydrophobic substrates: influence of surface properties. Colloids Interfaces 3(2). https://doi.org/10.3390/colloids3020048
91. Frandsen CJ, Brammer KS, Noh K, Connelly LS, Oh S, Chen L-H et al (2011) Zirconium oxide nanotube surface prompts increased osteoblast functionality and mineralization. Mater Sci Engineering: C 31(8):1716–1722. https://doi.org/10.1016/j.msec.2011.07.016
92. Lian H, Liu X, Meng Z (2018) Enhanced mechanical and osteogenic differentiation performance of hydroxyapatite/zein composite for bone tissue engineering. J Mater Sci 54(1):719–729. https://doi.org/10.1007/s10853-018-2796-0
93. Kaur K, Das S, Ghosh S (2019) Regulation of human osteoblast-to-osteocyte differentiation by direct-write 3D microperiodic hydroxyapatite scaffolds. ACS Omega 4(1):1504–1515. https://doi.org/10.1021/acsomega.8b03272
94. Komori T (2019) Regulation of proliferation, differentiation and functions of osteoblasts by Runx2. Int J Mol Sci 20(7):1694. https://doi.org/10.3390/ijms20071694
95. Matta C, Szucs-Somogyi C, Kon E, Robinson D, Neufeld T, Altschuler N et al (2019) Osteogenic differentiation of human bone marrow-derived mesenchymal stem cells is enhanced by an

aragonite scaffold. Differentiation 107:24–34. https://doi.org/10.1016/j.diff.2019.05.002

96. Shrestha S, Shrestha BK, Ko SW, Kandel R, Park CH, Kim CS (2021) Engineered cellular microenvironments from functionalized multiwalled carbon nanotubes integrating Zein/Chitosan @Polyurethane for bone cell regeneration. Carbohydr Polym 251:117035. https://doi.org/10.1016/j.carbpol.2020.117035